UNIVERSIDADE DE LISBOA

FACULDADE DE CIÊNCIAS

DEPARTAMENTO DE FÍSICA

Comparison of different image reconstruction algorithms for Digital Breast Tomosynthesis and assessment of their potential to reduce radiation dose

Raquel Silva Diogo

Mestrado em Engenharia Física

Dissertação orientada por:
Nuno Matela

2022

Agradecimentos

Abstract

Digital Breast Tomosynthesis is a three-dimensional medical imaging technique that allows the view of sectional parts of the breast. Obtaining multiple slices of the breast constitutes an advantage in contrast to conventional mammography examination in view of the increased potential in breast cancer detectability. Conventional mammography, despite being a screening success, has undesirable specificity, sensitivity, and high recall rates owing to the overlapping of tissues. Although this new technique promises better diagnostic results, the acquisition methods and image reconstruction algorithms are still under research.

Several articles suggest the use of analytic algorithms. However, more recent articles highlight the iterative algorithm's potential for increasing image quality when compared to the former. The scope of this dissertation was to test the hypothesis of achieving higher quality images using iterative algorithms acquired with lower doses than those using analytic algorithms.

In a first stage, the open-source Tomographic Iterative GPU-based Reconstruction (TIGRE) Toolbox for fast and accurate 3D x-ray image reconstruction was used to reconstruct the images acquired using an acrylic phantom. The algorithms used from the toolbox were the Feldkamp, Davis, and Kress, the Simultaneous Algebraic Reconstruction Technique, and the Maximum Likelihood Expectation Maximization algorithm.

In a second and final state, the possibility of further reducing the radiation dose using image postprocessing tools was evaluated. A Total Variation Minimization filter was applied to the images reconstructed with the TIGRE toolbox algorithm that provided the best image quality. These were then compared to the images of the commercial unit used for the image acquisitions.

With the use of image quality parameters, it was found that the Maximum Likelihood Expectation Maximization algorithm performance was the best of the three for lower radiation doses, especially with the filter. In sum, the result showed the potential of the algorithm in obtaining images with quality for low doses.

Key words: Digital Breast Tomosynthesis; Feldkamp Davis and Kress; Simultaneous Algebraic Reconstruction Technique; Maximum Likelihood Expectation Maximization; Total Variation Minimization.

Resumo

A Tomossíntese Digital Mamária é uma técnica tridimensional de imagem médica que possibilita a visualização de seções da mama. A obtenção de vários cortes da mama constitui uma vantagem deste tipo de técnica face à mamografia convencional pelo facto de ter o potencial de aumentar a detetabilidade do cancro da mama. A mamografia convencional, apesar do seu sucesso nos programas de rastreio de cancro da mama, apresenta problemas em especificidade, sensibilidade, e taxa de chamadas para repetição de exames devido à sobreposição de tecidos. A sobreposição de tecidos, que causa resultados falsos-positivos que necessitam de novos exames para reavaliação, mais exposição à radiação, custos e ansiedade aos pacientes, deixa de ser um problema com a tomossíntese. Apesar desta nova técnica ter o potencial para melhorar os resultados dos diagnósticos, o processo de aquisição e as técnicas de reconstrução de imagem ainda necessitam de ser otimizadas.

Existem duas grandes classes de algoritmos de reconstrução: analíticos e iterativos. Atualmente, em contexto clínico usam-se principalmente algoritmos analíticos. Contudo, estudos recentes salientam o potencial dos algoritmos iterativos em obter imagens de melhor qualidade para doses ao paciente mais baixas quando comparados com os outros. Este interesse em algoritmos iterativos cresceu com o desenvolvimento das *Graphics Processing Units* (GPUs) que permitiu, através da programação em paralelo, diminuir o tempo de reconstrução com algoritmos iterativos e por isso o seu uso em contexto clínico.

No âmbito desta dissertação foi por isso testada a hipótese do uso destes algoritmos em contexto clínico e analisada a qualidade de imagem para diferentes doses de radiação fazendo variar os fatores de exposição do tubo de raios-x. Foram comparados três algoritmos de recontrucao, um analítico e dois iterativos.

Para a reconstrução de imagem utilizou-se uma *toolbox open-source* desenvolvida em MATLAB, chamada *Tomographic Iterative GPU-based Reconstruction* (TIGRE) e um fantoma de acrílico com discos de alumínio. As medições foram realizadas no Hospital da Luz, em Lisboa, com um equipamento HOLOGIC. Foram realizadas várias aquisições para diferentes fatores de exposição (corrente de filamento e diferença de potencial entre ânodo e cátodo), por forma a caracterizá-las dosimetricamente. Repetiram-se as aquisições com os mesmos fatores de exposição, mas o fantoma com os discos de alumínio foi substituído por um fantoma que acomodava uma câmara de ionização para leituras de valores de kerma no ar para radiação na gama de energias da mamografia. Kerma é uma medida da energia cinética transferida da radiação para a matéria.

A *toolbox* utilizada neste trabalho, já tinha vários algoritmos desenvolvidos pela comunidade e pelo autor. Entre os quais foram selecionados três: *Feldkamp, Davis, and Kress*; *Simultaneous Algebraic Reconstruction Technique*; e *Maximum Likelihood Expectation Maximization*. O primeiro é um algoritmo, e os últimos dois são algoritmos iterativos. Em particular, o *Maximum Likelihood Expectation*

Maximization tem em conta a natureza estatística dos fotões quando interagem com a matéria, sendo por isso interessante de um ponto de vista físico.

A TIGRE *toolbox* tem algoritmos implementados com base em *General-Purpose computing on Graphics Processing Units* (GPGPU) bastante personalizáveis. Por isso, os parâmetros das funções dos algoritmos utilizados foram otimizados antes de se passar para a reconstrução. Em particular, no caso do algoritmo *Simultaneous Algebraic Reconstruction Technique*, o número de iterações necessário, tal como a ordem com que as projeções são escolhidas numa atualização do valor da imagem, como o parâmetro de relaxação do algoritmo foram avaliados. No caso do *Maximum Likelihood Expectation Maximization* foi necessário, além do número de iterações, considerar o uso de um filtro, uma vez que atualização do valor da imagem envolve uma operação de divisão. Para o *Feldkamp, Davis, and Kress*, apenas foi necessário escolher um filtro e a sua frequência de corte.

Uma vantagem da *toolbox* usada é que, apesar de ter sido desenvolvida para reconstruções de imagens de tomografia computadorizada, permite definir a geometria de um exame de tomossíntese. Esta foi definida tendo em conta a geometria do equipamento da HOLOGIC utilizado e que pode ser encontrada em manuais do equipamento e artigos científicos.

As imagens obtidas após reconstrução, foram analisadas utilizando três parâmetros de análise no plano onde os discos estavam focados: contraste, ruído e razão entre a diferença de sinal e o ruído.

Dos três algoritmos utilizados, o analítico foi o que apresentou níveis de ruído na imagem e valores de contraste mais elevados. Ambos os algoritmos iterativos se destacam tanto pelo nível de ruído e como de contraste baixo. Contudo, quando comparados utilizando a razão entre a diferença de sinal e o ruído, os resultados são diferentes. Mantendo o valor da corrente fixo ou o valor da tensão fixo, a razão entre a diferença de sinal e o ruído é mais elevada para os algoritmos iterativos. Em particular destaca-se o *Maximum Likelihood Expectation Maximization* para valores de corrente e de tensão que se traduzem em valores de kerma no ar mais baixos. A razão entre a diferença de sinal e o ruído é mais elevada.

Em termos do tempo de execução de cada algoritmo, como previsto, o *Feldkamp, Davis, and Kress* demorou menos tempo que os os dois algoritmos iterativos. Contudo, o *Maximum Likelihood Expectation Maximization* foi dos dois que demorou menos tempo por iteração e no total durante uma execução.

Numa segunda e última fase, fez-se uso de técnicas de pós-processamento com algoritmos 3D de minimização da variação total dos dados (TV, do inglês *Total Variation*). Estes filtros têm ótimos resultados na diminuição do ruído e na preservação das bordas das estruturas anatómicas. Aspetos importantes para um diagnóstico correto do tipo de cancro da mama.

As imagens reconstruídas com o algoritmo *Maximum Likelihood Expectation Maximization* foram pós-processadas com um destes filtros. O que foi utilizado nesta dissertação foi desenvolvido em MATLAB no âmbito de um trabalho de investigação realizado no Instituto de Biofísica e Engenharia Biomédica. O algoritmo inclui um estudo compreensivo de um parâmetro de regularização que determina o quão bem o algoritmo atua na imagem. Após serem processadas, as imagens foram comparadas com as imagens reconstruídas e pós-processadas pelo equipamento da HOLOGIC utilizando o mesmo tipo de análise realizado na primeira fase. O uso do filtro resultou numa notória diminuição no nível de ruído das imagens, sem que o valor do contraste alterasse. Quando comparados tanto os resultados com e sem a aplicação do filtro, as imagens processadas pelo sistema da HOLOGIC tem os níveis de ruído e de contraste mais elevados. Contudo, mais uma vez, quando comparados utilizando a razão entre a diferença de sinal e o ruído, o *Maximum Likelihood Expectation Maximization* com e sem filtro

apresentou valores mais elevados para valores de kerma no ar baixos. Com o filtro, o aumento da razão entre a diferença de sinal e o ruído aumentou quase três vezes e em comparação com as imagens da HOLOGIC os resultados são em média cinco vezes mais elevados.

O facto de ter sido possível obter estes resultados através do uso de algoritmos iterativos, em particular com o *Maximum Likelihood Expectation Maximization* é muito interessante principalmente por mostrar resultados particularmente bons para valores de kerma no ar baixos. Em suma, o uso deste tipo de algoritmo e de algoritmos de minimização total da variação dos dados podem potencialmente permitir a redução de dose de radiação em Tomossíntese Digital Mamária.

Palavras-chave: Tomossíntese Digital Mamária; *Feldkamp Davis and Kress*; *Simultaneous Algebraic Reconstruction Technique*; *Maximum Likelihood Expectation Maximization*; Minimização da Variação Total dos Dados.

Table of Contents

List of Figures

List of Tables

List of Acronyms

3D	Three Dimensions
AEC	Automatic Exposure Control
Ag	Silver
Al	Aluminium
ART	Algebraic Reconstruction Technique
a-Se	Amorphous Selenium
BC	Breast cancer
BP	Backprojection
CBCT	Cone Beam Computed Tomography
CNR	Contrast to Noise Ratio
COR	Centre of Rotation
CT	Computed Tomography
CUDA	Compute Unified Device Architecture
DBT	Digital Breast Tomosynthesis
DICOM	Digital Imaging and Communications in Medicine
DQE	Detective Quantum Efficiency
DSD	Distance Source Detector
DSO	Distance Source Object
EM	Expectation Minimization
FDA	Food Drug Administration
FDK	Feldkamp Davis and Kress
FFDM	Full Field Digital Mammography
GPGPU	General-Purpose computing on Graphics Processing Units
GPU	Graphics Processing Units
IBEB	Institute of Biophysics and Biomedical Engineering
IR	Iterative Reconstruction
MEX	MATLAB Executable
ML	Maximum Likelihood
ML-EM	Maximum Likelihood – Expectation Minimization
Mo	Molybdenum
PMMA	Polymethyl Methacrylate
Rh	Rhodium
RMSE	Root Mean Square

ROI	Region of Interest
SAA	Shift-And-Add
SART	Simultaneous Algebraic Reconstruction Algorithm
SDNR	Signal Difference to Noise Ratio
TFT	Thin Film Transistors
TIGRE	Tomographic Iterative GPU-based Reconstruction
TV	Total Variation
W	Tungsten

CHAPTER 1

Introduction

Breast cancer (BC) is the most frequent oncological disease in women worldwide, Fig. 1.1. In Portugal, 7 000 new cases of breast cancer are detected annually, and 1 800 women die of this disease [1].

Top cancer per country, estimated age-standardized mortality rates (World) in 2020, females, all ages
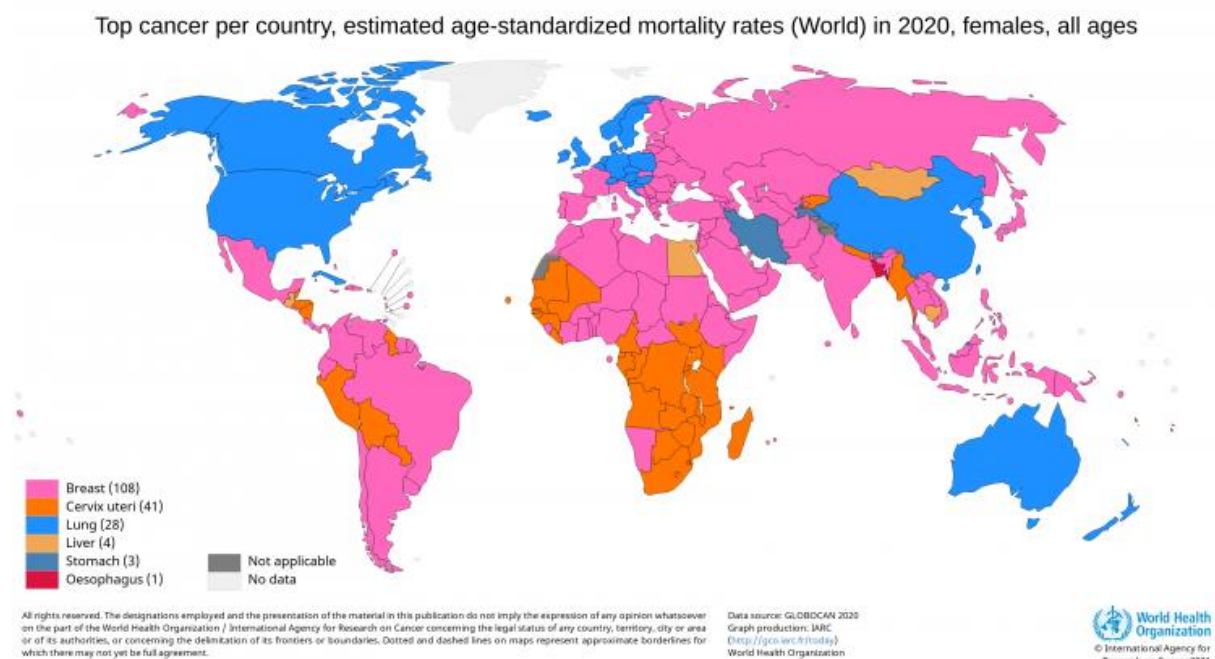
Figure 1.1 Map showing the top cancer mortality rates per country in 2020 for females of all ages. Source WHO.

In 2020, despite the global pandemic situation, during which fewer people went to hospital afraid of the virus and the quarantine periods, there were 2.3 million women being diagnosed with BC and 685 000 deaths globally. Moreover, it is the world's most prevalent cancer. By the end of the year, 7.8 million women, who were diagnosed with this type of cancer, were alive. In every country, it affects women at any age after puberty, with increasing rates in later life (> 65-year-old), Fig 1.2. Mortality rates started changing in the 1980s in countries that had early mammography detection programmes combined with different modes of treatment. These forms of treatment can be highly effective, especially when the cancer is identified early [2].

Estimated age-standardized incidence rates (World) in 2020, breast, all ages

ASR (World) per 100 000

≥ 69.2
53.0–69.2
41.1–53.0
30.3–41.1
< 30.3

Not applicable
No data

World Health Organization
© International Agency for Research on Cancer 2021
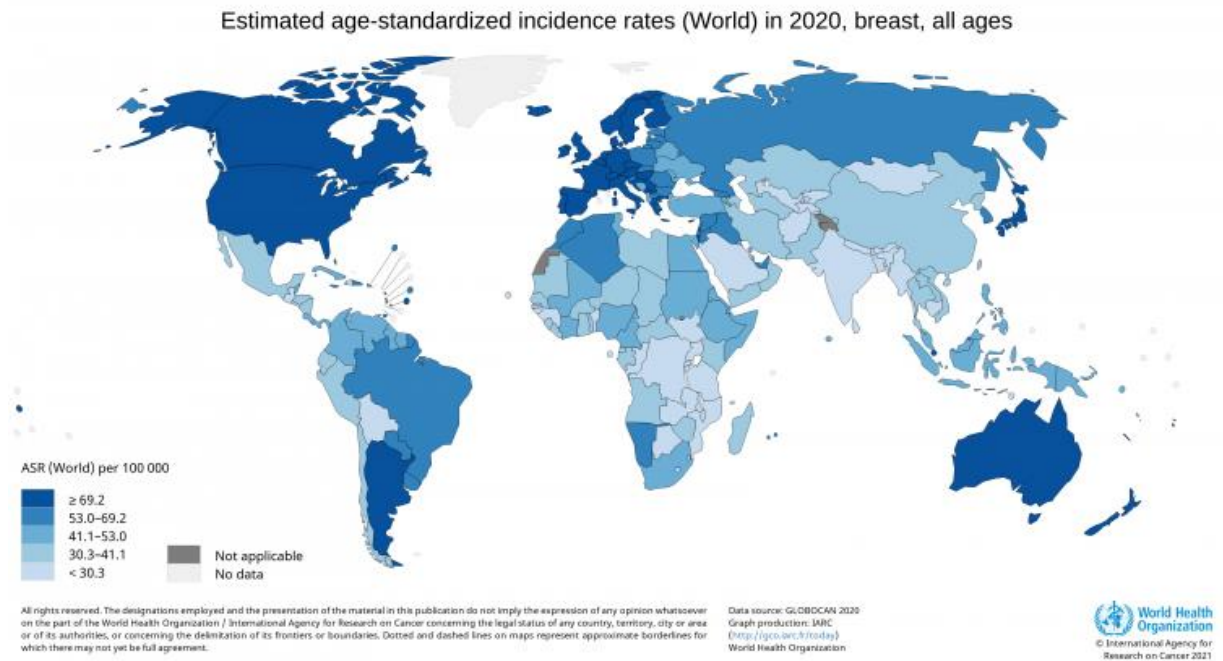
Figure 1.2 Map showing incidence rates of breast cancer per country in people of all ages. Source WHO.

Dose reduction in imaging with ionizing radiation has been an increasing concern lately due to its potential risk of causing radiation-related cancers. Hendrick [3] evaluated a series of studies about cancer risk and radiation doses, in 2010. On average, approximately 10% of women in the US are recalled after screening mammography. As a result, the population dose and risk are increased, on average, an additional 5%-10%.

In 2011, the Food and Drug Administration (FDA), approved the use of a new promising imaging modality called Digital breast tomosynthesis (DBT). The purpose of this work is to investigate the impact of image reconstruction algorithms and post-processing methods on the final image quality of DBT.

This work is divided in 7 chapters, being this introduction the first. In the second chapter, a short introduction to the theoretical aspects of x-ray production and its interaction with matter will be presented. In the third chapter, the DBT imaging technique and its advantages, disadvantages and state-of-the-art are going to be clarified. This is followed by a chapter explaining how the final DBT image is obtained and some comparison between the methods described and used in the research work of this thesis. In the fifth and sixth chapters, the materials, results, and discussion of the research work on the reconstruction algorithms and post-processing of the DBT images are presented. Finally, in the seventh chapter, we conclude this dissertation with the main findings.

CHAPTER 2

Theoretical Considerations

2.1 Production of X-rays

2.1.1 X-ray Spectrum

Modern medical imaging examinations are possible thanks to the discovery of x-ray radiation by Wilhelm Conrad Roentgen in 1895, who observed a new type of radiation being emitted from his cathode-ray tube.

This tube converts the kinetic energy of electrons into electromagnetic radiation, i.e., x-rays, by accelerating those electrons in a potential difference inside a vacuum chamber. A high voltage is applied to the cathode, negative potential, which heats and emits from its surface electrons by a process called thermionic emission. These electrons are accelerated and then interact with a target material, the anode, generating X-rays radiation: bremsstrahlung radiation, and characteristic radiation that compose the so-called X-ray spectrum, Fig 2.1.
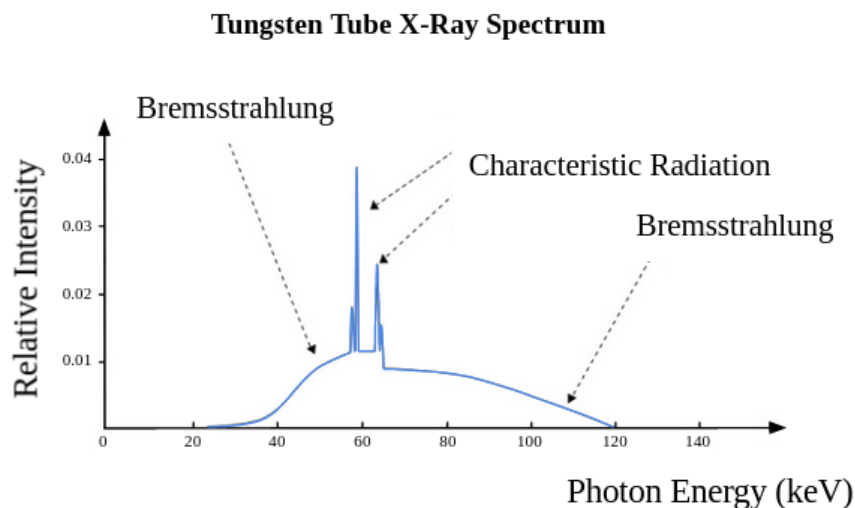
Figure 2.1 X-ray spectrum of a tube with a Tungsten (W) anode. Adapted from [4].

X-ray Production
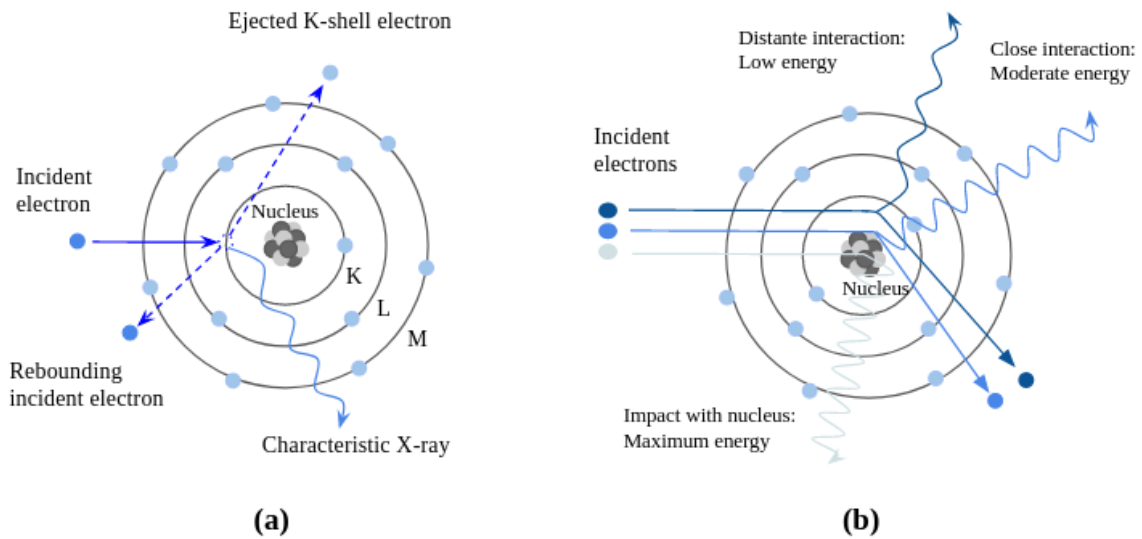
Figure 2.2 X-rays are produced from the interaction of an electron with a material. There are two possible scenarios: (a) a characteristic x-ray is produced, (the incident electron has kinetic energy higher than the binding energy of the electron in the K-shell, and therefore, after the collision, the incident electron is scattered while the K-shell is ejected); or (b) bremsstrahlung radiation is produced (the incident electron interacts with the nucleus and is decelerated losing energy in the form of radiation). Adapted from [5].

The first is a consequence of the deceleration by the interaction with the target material due to the Coulombic force that attracts the electron to the nucleus, deflecting it. This makes the electron "lose" energy, which is emitted as a photon, i.e., bremsstrahlung radiation (from the German, meaning "braking radiation"), Fig. 2.2. (b) The generation of bremsstrahlung x-ray depends on the atomic number, Z, of the target material - being higher for high atomic number materials -, and potentials - higher the potential, higher the rate of production. The last portion of the energy is not irradiated as bremsstrahlung x-rays but is spent in ionisation and excitation by collision interactions. Thus, it will be dissipated as heat, meaning that special care needs to be taken when choosing the target and designing the tube.

The second process happens when the electron with kinetic energy exceeding the binding energy of an electron from the inner shell, K-shell, collides with it. The K-shell electron is then ejected, while the other is scattered, creating a hole that is filled with an outer shell electron, Fig. 2.2. (a) It can only be filled by an L-shell (K_α radiation) or the M-shell (K_β radiation) electron. Energies are further split owing to the energy levels in a shell, indicated with a numerical suffix. The energy of this radiation is characteristic to the atom, since it is equal to the difference in the electron binding energies of the initial and final states for the transition, which depends on atomic number.

2.1.2 X-ray Tube

To produce x-rays, the main components are the filament and a focusing cup serving as the tube's cathode, the target or anode, the tube envelope in vacuum, and the high voltage supply, see Fig.2.3.
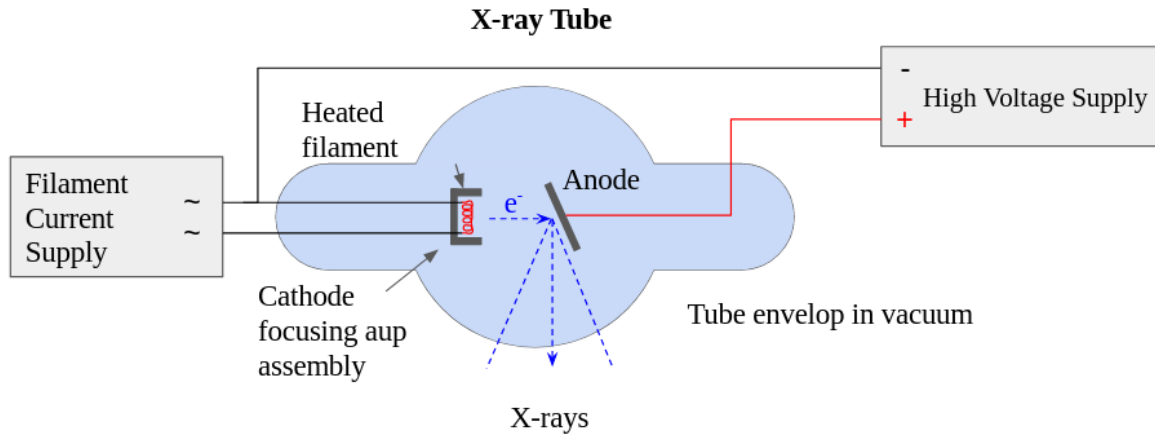
Figure 2.3 X-ray tube main components. Adapted from [5].

The tube voltage (kV), current (mA), and exposure time are the three major selectable parameters on the X-ray generator control panel. These determine the x-ray beam characteristics, together with the selection of the target. Often the tube current and exposure are given as one quantity, the product of the current and the exposure time (mAs).

Tube voltage will determine the maximum energy of the bremsstrahlung spectrum, the efficiency of X-ray production, and the quality and quantity of photons generated. On the other hand, the current, which is determined by the filament current, will affect only the efficiency of X-ray production. For both tube voltage and current increase, for a constant tube current and tube voltage respectively, the radiation dose will increase, Fig. 2.4.
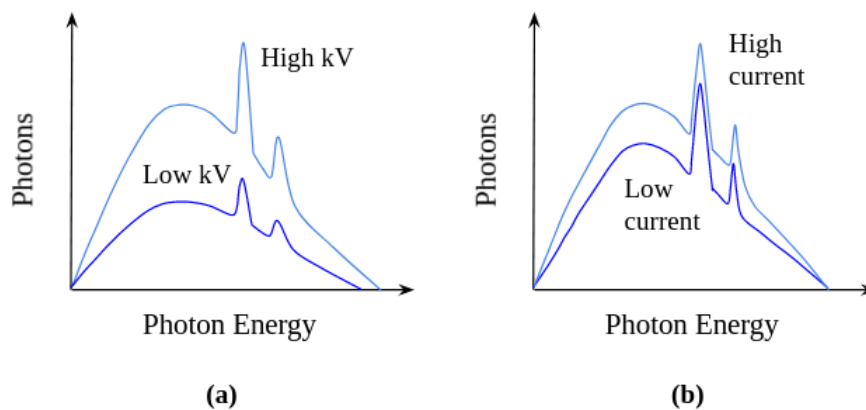
Figure 2.4 Effect of the X-ray tube voltage (a), and tube current (b) on the X-ray spectrum generated. By increasing the voltage, the quantity and of the photon as well as their average energy is increased.

The x-rays will not be as easily absorbed in the patient's body, therefore, increasing the number of photons that contribute to image formation and the dose to the patient. If the current is higher, only the quantity of generated photons will increase.

The anode material will influence the spectrum emitted from the x-ray tube. In general, the anode for radiography applications should be chosen such that it has a high bremsstrahlung yield, meaning that materials with high atomic numbers, Z, are preferable. Tungsten (Z = 74), W, is the most widely used material. Although, in mammography, Molybdenum (Z = 42), Mo, and Rhodium (Z = 45), Rh, targets are used because of their dominant characteristic x-rays and low bremsstrahlung contribution allowing a more satisfactory optimization of image quality and patient dose.

The anode material and configuration are also chosen taking into consideration the low efficiency of x-ray production. In fact, only approximately 1% is x-ray radiation, the rest is thermal energy. Meaning that heat conduction and heat capacity are important physical properties to take into consideration when choosing a material for the anode.

Beyond these components, x-ray filtration needs to be taken into consideration since it can be used to control the quantity and the quality of the x-rays. It includes both the inherent tube filtration and the added filtration. By filtering out the low energy part of the spectrum, which can be absorbed in the patient and thus not contribute to image formation, the radiation dose to the patient is reduced. The removal of low energy x-rays increases the average photon energy and penetration (beam hardening). Aluminium (Al) is the most used filter. Mo, Rh, and silver (Ag) are also currently used in applications, like mammography.

2.2 X-ray Interactions with Matter

Diagnostic medical imaging is only possible due to the interaction of the particles with matter. X-rays, uncharged monoenergetic particles, incident on a material of thickness, x, whose initial energy fluence is Ψ_0, will be attenuated according to the exponential law given by

$$\Psi = \Psi_0 e^{\mu x} \qquad\qquad \textbf{Equation 2.1}$$

The quantity μ is called the linear attenuation coefficient, which divided by the density of the attenuating medium, $(\mu/\rho)_{med}$, is called the mass attenuation coefficient. However, this is only true if no secondary radiation is produced, that is if we have narrow-beam attenuation. When interacting with matter, photons generate either charged or uncharged secondary radiation, or scattered primary radiation. It is said that, in this case, we have broad-beam attenuation. Consequently, the attenuation coefficient will be higher. To have narrow-beam geometry one can simply place a collimated source at a sufficiently large distance from the attenuating material. The intensity of the secondary particle will decrease with the inverse squared of the distance, and the primary particles will be almost perpendicularly incident.

There are four fundamental x-ray interactions in medical imaging: photoelectric effect, incoherent (Compton) scattering, coherent (Rayleigh) scattering, and pair production. The importance of each of these interactions depends on the atomic number of the absorbing medium as well as the photon energy. The previously mentioned linear attenuation coefficient is the sum of the individual linear attenuation coefficients for each type of interaction (see Fig. 2.5).

Mass Attenuation Coefficient for Soft Tissue
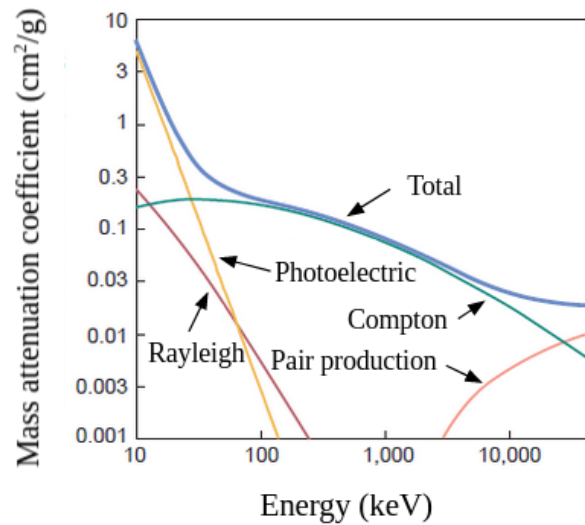
Figure 2.5 Graph of the Rayleigh, Compton, photoelectric, pair production, and total mass attenuation coefficients for soft tissue (Z = 7) as a function on photon energy [5].

In the range of x-ray energies used in mammography, the photoelectric and the Compton scattering interactions are the most dominant.

During a photoelectric interaction, an incident photon excites the atom, transferring all its energy to an electron, which is then ejected with a kinetic energy equal to the difference in binding energy and photon energy. This vacancy is filled with the emission of either a characteristic x-ray or an Auger electron.

There is a strong relation between the atomic number and the photon energy with the photoelectric effect mass attenuation coefficient, for the energies used in x-ray diagnostics, $\{\sim Z/(h\nu)\}^3$. Although the mass attenuation coefficient decreases, in general, with increasing photon energy, there are, for every element, sharp discontinuities called absorption edges. This happens because the photon energy might just exceed the binding energy of inner-shell electrons, thus increasing the number of electrons available for interaction. The photon energy at the absorption edges is the binding energy of the electrons in that shell or subshell.

In Compton scattering, the photon interacts, most likely, with an outer-shell electron (free electron), resulting in the ionization of the atom and a division of the incident photon's energy between the scattered photon and the electron, which is ejected from the atom. The Compton effect does not depend on the atomic number but on the material's density.

Because those two interactions are dominant in the range of the mass attenuation of the soft tissue, they are particularly important in breast medical imaging applications. The higher the photon energy, the more likely photons are to travel through the patient without any interaction, consequently generating images with poorer contrast.

CHAPTER 3

Breast Imaging

3.1 Mammography

Until now the most important and reliable breast imaging technique has been x-ray mammography. During this exam, the breast is compressed and an x-ray beam of radiation transverses the breast until it reaches a detector or film (Fig. 3.1), depending on if it is digital or film mammography, respectively. One or two views of the breast can be performed, and with focus on specific areas of the breast.
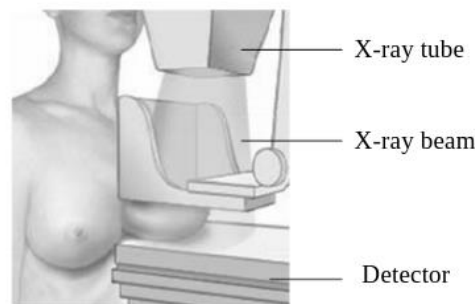
Figure 3.1 Mammographic acquisition representation. Adapted from [6].

Several randomised clinical trials carried out over the years, by different organisations across the world, have shown that mammography screening is associated with a reduction in BC mortality, especially for women in the 50-69 age gap [7]. However, this low dose x-ray non-invasive exam has its shortcomings in sensitivity and specificity. This can lead to undesirable effects such as recalling for further investigations because of a false positive result, which is especially common in women with denser breast. Consequently, the patient experiences significant anxiety, which can have greater negative effects if a biopsy is required. On top of this, overlapping of tissues can mask tumours [8-9].

3.2 Digital Breast Tomosynthesis

3.2.1 Developments, Advantages, and Disadvantages

The theoretical framework for tomosynthesis, or limited angle tomography, was early introduced by Ziedses des Plante [10], and only truly possible to implement with the development of flat-panel detectors in the 1990s [11]. With this new detector technology, the acquisition of low-dose projection images was possible at reasonable speeds needed, thanks to its detective quantum efficiency (DQE) [12-13]. Digital breast tomosynthesis (DBT) has been continuously studied as an alternative or complementary breast cancer screening exam to conventional mammography. The advantage of DBT is that it allows cross sectional visualisation of the breast tissue, see Fig. 3.2, which in turn removes the difficulty in detecting certain lesions due to the superposition of tissue present in a projection mammogram [8-9,14].

Studies have shown that it can reduce the recall rates [18-19], improve cancer detection in women with dense breast tissue, and improve the distinction between benign and malignant lesions [15-19,23]. As seen by Andersson *et al* [17], breast tomosynthesis rates of visibility are higher than those in digital mammography, and lesions can also be more accurately classified using the Breast Imaging Reporting and Data System (BIRADS) of classification, Tab. 3.1, indicating a potential increase in sensitivity. Moreover, using a combination of DBT and Full Field Digital Mammography (FFDM) was shown to result in a 30% reduction of recall rate for cancer-free examinations (false positives) compared to the conventional FFDM [19]. Smith *et al* [20] showed that, regardless of their experience, radiologists performance benefited from DBT when used in adjunction to FFDM.

Overall, DBT could reduce the number of biopsies, and the degree of compression of the breast contributing to an overall wellbeing of the patients [22-23]. Besides, a one view tomosynthesis image at the same dose as standard screen-film mammography is non-inferior to digital mammography [16]. All contributing to the possibility to reduce the cumulative dose to the patient by avoiding unnecessary additional exams.

However, some studies state there is no convincing evidence that DBT alone or in combination with FFDM results in a sensitivity improvement [18]. Furthermore, microcalcification detectability is reported to be inferior to that of FFDM [15, 24-25], plausibly due to DBT's anisotropic resolution. In a pilot study with 98 patients, of which 14 cases of microcalcification were identified, Poplack *et al* [15], reported that in 29% of the cases the microcalcification where equally well seen on digital mammography and tomosynthesis, in 57% of the cases were better seen in digital mammography, and 14% were better seen in DBT. Not to mention that compared with FFDM, tomosynthesis suffers from blurring because of the tube's motion, long time of acquisition, and detector characteristics [24]. Moreover, contrary to other studies, Teertstra *et al*, using a two-view tomosynthesis diagnostic study of 513 women, demonstrated no significant difference in sensitivity or specificity between FFDM and tomosynthesis [26].

Table 3.1 BIRADS classification according to the American College of Radiologists [21].

BIRADS Classification	Description
1	Negative
2	Benign finding
3	Probably benign
4A	Low suspicious abnormality
4B	Medium suspicious abnormality
4C	High suspicious abnormality
5	Highly suggestive of malignancy

   Other issue with DBT is the dose to patients. When a combined FFDM/DBT study was performed the dose was on average 2.8 times higher than the one obtained for a single FFDM view [27]. On top of this, more and more the cumulative dose has been a concern for the health specialists that want to reduce it to further reduce the risk of radiation dose induced cancer.

3.2.2 System Geometry

   Most DBT systems consist of an x-ray tube mounted in an arm, a direct or indirect full field digital detector, and a breast support plate with a compression plate. Contrary to the mammography system, the DBT system's x-ray tube rotates around a point close to or on the detector, Fig. 3.2.

Diagram showing a tomosynthesis system geometry
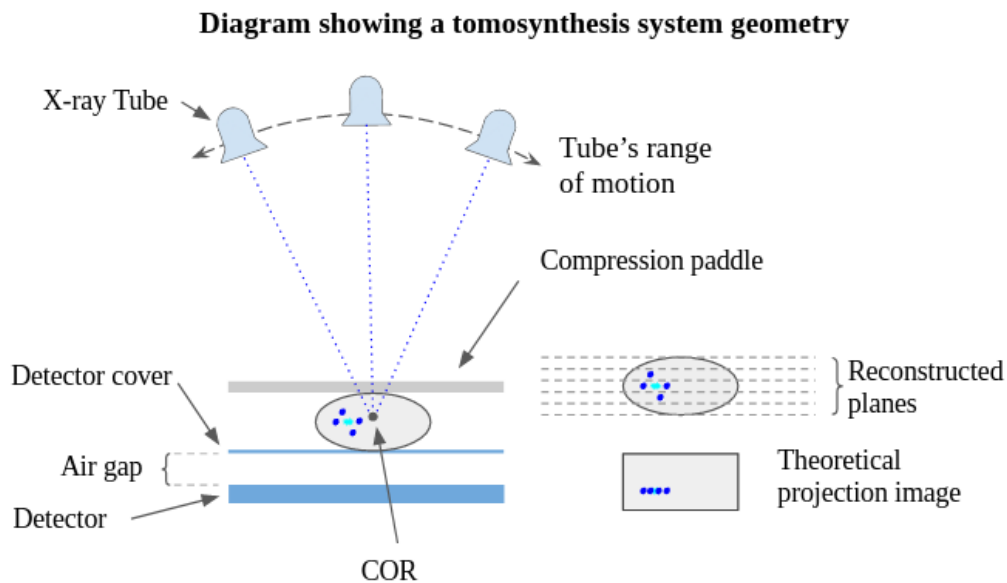
Figure 3.2 Diagram of a tomosynthesis system geometry. The X-ray tube covers an arc of an angle with the centre of rotation (COR) either on the detector or somewhere within the breast being imaged. A com-pression paddle ensures that the breast stays immobile during the exam. A direct or indirect detector, which can be static or rotate, is located either immediately after the detector cover or has an air gap between them.

In almost all current DBT systems, the partial isocentric geometry of motion, where the detector stays fixed beneath the breast, is used due to its manufacturing simplicity, Fig. 3.3 (b). However, the tube and detector can also rotate together around a fixed point (isocentric or Grossman geometry), Fig. 3.3 (a).

DBT Commun Geometries of Motion

(a) Isocentric   **(b) Parcial Isocentric**
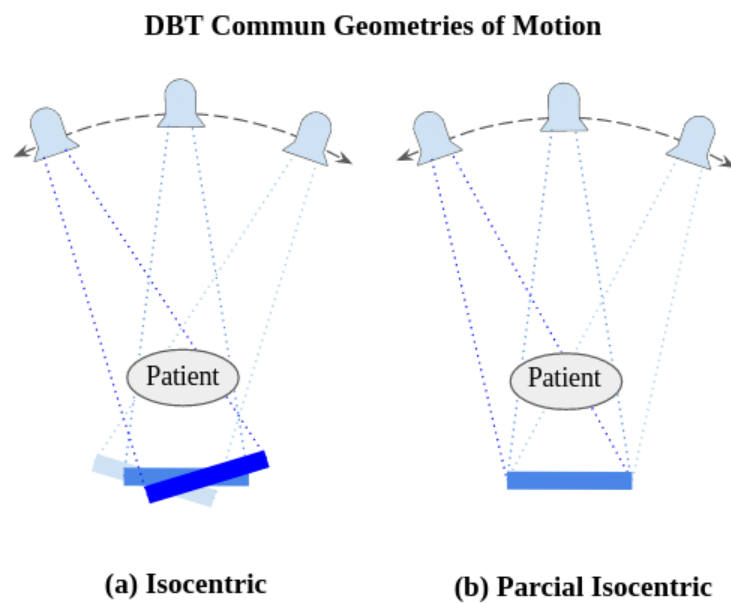
Figure 3.3 Geometry of a DBT system.

The x-ray tube's motion can either be continuous (short x-ray pulses are used to avoid blurring the image), or step-and-shoot (gantry stops at each angular location before turning on the x-ray tube, otherwise vibration will blur the image). The motion can lead to motion-related blurring of small structures, like microcalcifications, due to the oblique incidence of x-rays on the detector [28-29]. Moreover, the pattern of distribution of some calcifications can be more difficult to appreciate in section imaging, unless a relatively thick section is used.

The detectors used, which made possible the development of DBT, are digital. Flat panel detector arrays, that became available in the mid to late 1990s, are the major detector technology used in DBT. A matrix composed of thin film transistors (TFT) arrays collects the electrical charge generated during the x-ray exposure, absorption, and conversion process; stores the charge in a capacitor attached to each element; and actively reads each array. There are two main detector technologies: indirect and direct x-ray conversion.

Although, the most used is the second. A layer of semiconductor, amorphous selenium (a-Se), is added to the TFT array. This material, when an incident x-ray is absorbed, will directly produce electron-hole pairs.

3.2.3 Image Acquisition and Reconstruction

During the tube's movement, numerous projection images are obtained, and then, using reconstruction algorithms, combined to produce thin-slice cross-sectional images or an estimated 3D image distribution of the breast tissue. The image is then stored in computer memory and can be further processed.

Parameters that must be set during acquisition are the tube voltage, tube current, anode target and filter materials, exposure time per projection, degree of compression, number of projections, and total angular range. The last two are only applied to DBT. As such, these have been the most researched acquisition parameters since there are no previously established modalities that involve similar parameters from which to draw any experience.

Since the projection images are not acquired over a full 360° rotation about the patient, the resolution in the z direction, i.e., in the direction perpendicular to the x-y plane of the projection images, is limited. Thus, tomosynthesis does not produce the isotropic spatial resolution achievable with computed tomography (CT). The resolution is better in the planes parallel to the detector, and lower in the perpendicular direction [30]. On top of this, the choice of total angular range and number of projections highly impacts the resulting image quality. Chawla *et al.* [31] concluded that, if angular range is kept constant, the best performance is achieved at a higher dose, and that if the number of projections is kept constant, an increase in the angular range translates into a better performance. The number seems to be independent of the dose level. On top of this, results showed that increasing the number of projections up to a threshold does not further improve the vertical resolution. These results agreed with the ones obtained by Sechopoulos and Ghetti [32], that also found that the in-plane image quality is inversely proportional to the number of projections under a constant dose condition, agreeing with the findings of Ren *et al.* [33]. Van de Sompel *et al* [34] analysed the aspects affecting image

quality in DBT and found that the contrast to noise ratio (CNR) was improved for small microcalcification for narrow acquisition but did not change significatively for larger calcifications. In this study, the image quality difference between rotating and static detector acquisition geometry was also investigated. It was found that rotating detectors' CNR improved, when filtered backprojection, and maximum likelihood reconstruction algorithms were used. In sum, there is a trade-off between the number of projections and exposure per projection or angular range with spatial resolution. If the number of projections is increased, the exposure per projection must be lowered to guarantee an acceptable value of glandular dose, at the expense of an increase in quantum noise in each projection.

Tube current - exposure time distribution can be uniform during the acquisition or, as was proposed by Nishikawa *et al* [35], be non-uniform. In their study, Hu and Zhao [36] show that a variable acquisition can be advantageous in the detection of small microcalcifications, especially if a higher dose is delivered towards the central view of a tomosynthesis scan while reducing the dose at the periphery.

3.2.4 State-of-the-art of Tomosynthesis Systems

There are several commercial and prototype systems now, whose characteristics vary from manufacturer to manufacturer. The only FDA approved systems are GE Senographe Pristina, Fujifilm ASPIRE Cristalle, Siemens MAMMOMAT Inspiration, GE SenoClaire Digital Breast Tomosynthesis, and HOLOGIC Selenia Dimensions. Philips Healthcare MicroDose prototype system is the one that mostly differs from the others. This system is based on a scanning slip photon counting detector, and provides a very low scatter signal, no electronic noise, and high quantum efficiency. Some units now have dual functionality, i.e., perform both two-dimensional digital mammography and breast tomosynthesis, like the Hologic DBT system [37]. Other optimizations implemented by the manufacturers to their systems include different x-ray spectrum filtration and pixel binning [37-38].

The optimal reconstructed section thickness, and the appropriate use for this technology (screening, diagnostic) are some of the issues yet to be solved. In addition, some studies will have to be done to determine the benefits of doing two view examination in improving sensitivity and, maybe, specificity. In any case, determining the optimal imaging technique and clinical role of DBT translates into radiation dose issues. Although, breast tomosynthesis holds promise for future applications in estimating tumour volume, contrast-enhanced 3D imaging, multifocal or multicentric disease evaluation for surgical planning, 3D guided procedures with lesion depth information, and computer aided diagnosis [39].

CHAPTER 4

Image Reconstruction

4.1 Image Reconstruction Problem

The volume to be reconstructed can be divided into several cubic units called voxels that have an attenuation coefficient associated and which we want to estimate (inverse problem). The pixels from the projection data will represent the line integral along the path of the ray that crosses the "voxelized" object, from the x-ray source to the detector. Therefore, each voxel crossed by that ray contributes to the attenuation of the photons that reached that detector pixel.

We can think of the reconstruction problem as an undetermined linear system of equations. The value of the attenuation coefficient of each voxel will be calculated from the pixel values of the projection data. Mathematically,

$$Y = Ax + \eta \, , \qquad \textbf{Equation 4.1}$$

where Y is the measured data, A the system matrix, x the image to be estimated, and η addictive noise which in DBT can be scattered x-rays and electronic noise. The system matrix describes the probability of a photon to be absorbed by a voxel. For simplicity, the addictive noise will be neglected. The system matrix calculation is independent of the reconstruction algorithm used.

Let the linear attenuation coefficient for the voxel v be x_v, $1 < v < V$, the number of pixels be denoted by p, $1 < p < P$, and n be the projection number, $1 < n < N$. The reconstruction problem can be described by the Eq. X

$$A_n x = Y_n \, , \qquad \textbf{Equation. 4.2}$$

where A_n is the projection matrix for the n-th projection with $a_{vp,n}$ as its (p,v)-th element, and y_n is the projection data obtained from the pixel value of the image. Meaning that, considering each individual projection, for a pixel p,

$$y_{p,n} = \sum_v a_{p,v} \, x_v \, . \qquad \textbf{Equation 4.3}$$

According to the Beer-Lambert law, the projection data $y_{p,n}$ is proportional to the logarithmic transform of the ratio of the incident intensity, $I_{i,n}$, and the transmitted intensity, $I_{o,n}$, of the ray on that pixel,

$$y_{p,n} = k\,ln\left(\frac{I_{o,n}}{I_{i,n}}\right)$$

<div align="right">**Equation 4.4**</div>

The natural logarithm of the ratio of the incident photons and the outgoing photos is known as ray sums. With this, a gray scale level is attributed to different tissues in the breast.

To solve Eq. 4.2., at least one operation is required: Ax (forward projection), and A^Ty (backprojection). Moreover, from Eq. 4.4, the data needs to be logarithmically transformed before any operation is used.

4.1.1 System Matrix Calculation

As mentioned in the previous section, the volume is divided into voxels whose linear attenuation coefficients will be estimated from the pixel data. To each pixel, a straight segment from the X-ray source to the centre of the pixel is traced. The line will cross multiple voxels and each voxel will contribute to the attenuation coefficient of that photon. To determine the probability of a voxel to attenuate a photon the estimation of the length of the path crossed by the photon within the voxel is used.

In 1984, Siddon proposed a way to calculate the exact radiological path for a 3D CT array [40]. Voxels are considered as intersection volumes of orthogonal sets of equally spaced parallel planes. First, the intersections of all rays with the planes are computed, followed by the distances between all consecutive intersections and all the coordinates of all voxels, Fig.4.1.

Ray Tracing Illustration
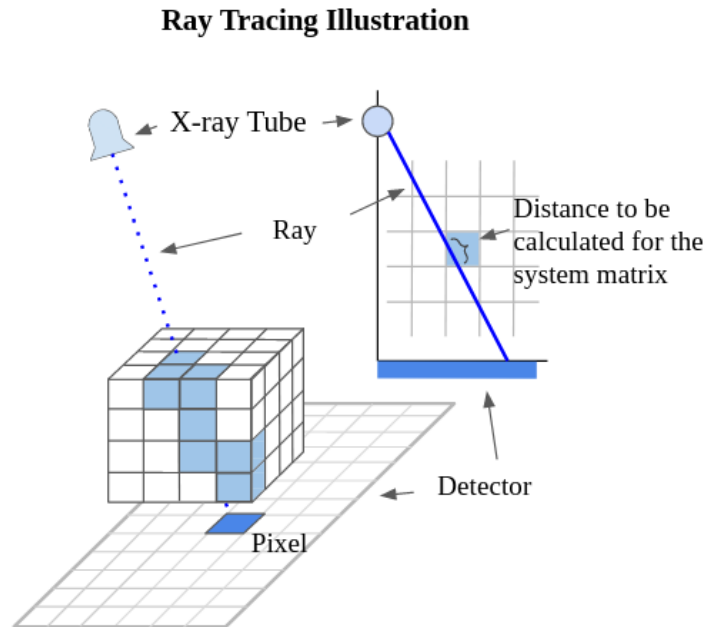
Figure 4.1 Diagram illustrating the intersection of a ray from an X-ray tube and the detector's pixel. Only the voxels crossed by the ray are contributing to the photon's attenuation.

4.2 Tomosynthesis

Tomosynthesis is mostly explained as a technique of generating slice images from the summation of a set shifted projection images acquired at different orientations of the tube. This Shift-And-Add method (SAA), Fig. 4.2, was the earliest tomosynthesis reconstruction algorithm used to attempt image reconstruction. Due to the motion of the tube, objects at different heights above the detector will experience different degrees of parallax, and thus be projected onto the detector at positions depending on the relative heights of the objects. With the SAA algorithm, projection images are used to generate a plane focused on a certain depth in the breast.
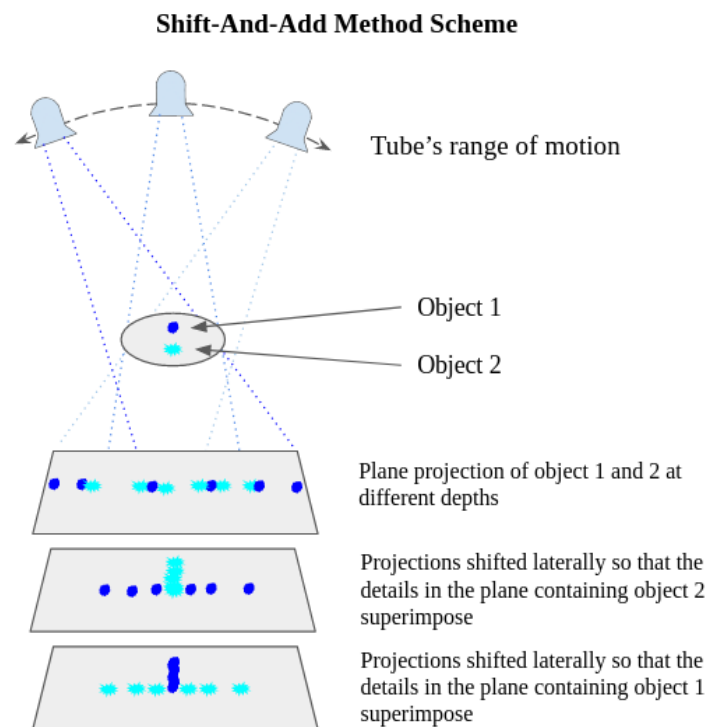
Figure 4.2 Scheme showing how the projections were shifted and added to make visible two different objects at different depths. Adapted from [41].

However, many more algorithms have been developed and improved to perform tomosynthesis image reconstruction. They can be divided into two major classes: algebraic or analytic. The algebraic algorithms can be further classified as either statistical or algebraic, Fig. 4.3. The algorithm choice is critical as it affects the image quality.

Recent surge in computational power, awoke the interest in iterative reconstruction (IR) algorithms. With the advances in GPU-based hardware, including an increasing number of computing cores and amount of memory, reconstruction time has been dropping, a major issue with IR algorithms. The studies on the use of such algorithms, mainly in CT applications, have shown to afford a reduction in

dose due to a more precise modelling of the acquisition process. Moreover, these methods represent a more intuitive and natural image reconstruction technique as they include various physical models. Counting statistics of detected photons are modelled by respective weighting of the measured rays, and some implementations include the modelling of the image acquisition geometry or incorporate additional information on the x-ray spectra used.

This work will focus on the comparison between one of each of the algebraic iterative, algebraic statistical, and analytical algorithms. Namely, the FDK, SART, and ML-EM algorithms, Fig. 4.3, will be further explained in the following sections.
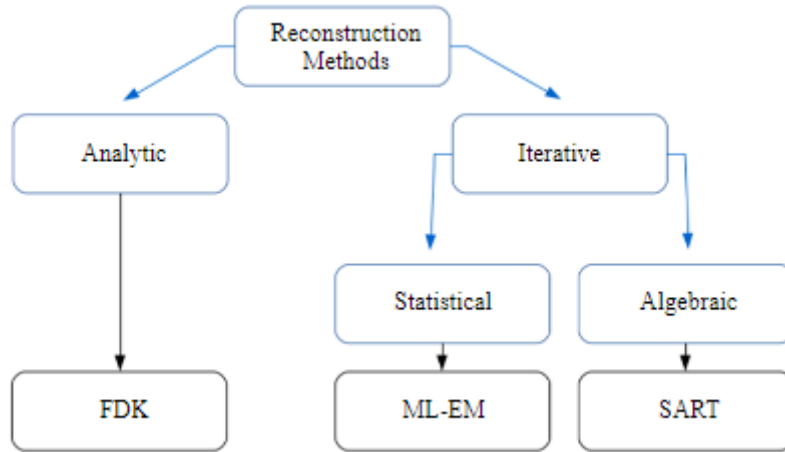
Figure 4.3 Reconstruction methods categories, and algorithms used (FDK, ML-EM, SART).

4.3 Analytical Methods

4.3.1 Filtered Backprojection

The Fourier slice theorem can be used to transform the projection images onto the spatial frequency domain. The 2D Fourier transform of each projection image corresponds to one slice sample in the spatial frequency domain at the corresponding angle. After acquiring several projections, we can represent the full Fourier representation of that object. Then, an inverse Fourier transform can be applied to obtain the object.

The simple backprojection gives blurry images since low frequencies are oversampled compared to high frequencies. In addition, in DBT, the frequency space is under sampled. A way to eliminate this is to apply a filter to the image. This method is known by filtered backprojection (FBP). Feldkamp, Davis and Kress proposed in 1984 [42] an approximate reconstruction algorithm for circular 3D cone-beam tomography. This algorithm is commonly called FDK.

There are three steps in the algorithm. First, the projections are scaled as if they were measured at the plane containing the isocenter. Then, the projections are filtered in the frequency domain, which exchanges the computationally expensive convolution process by a multiplication of two functions. Different filters can be used, namely, a ramp filter, a Hamming filter or a Hanning filter. Finally, the projection data is backprojected over a grid to reconstruct the object.

Mathematically, the approximate solution described above,

$$f_{FDK}(x,y,z) = \int_{-\theta}^{\theta} d\theta \frac{1}{U^2} \times \int_{-\infty}^{\infty} p(\theta,u,v') \frac{D}{\sqrt{D^2+u^2+v'^2}} \cdot h(u'-u) \cdot du d\theta,$$

Equation 4.5

where p(θ, u, v') is the projection measured in the detector at every tomographic angle θ, h(•) describes the filter, u and v are the coordinates in the plane of the projection space, R the distance between the source and the centre of rotation, D the source to detector distance, and

$$u'(x,y,\theta) = \frac{D(y\cos\theta + x\sin\theta)}{R + y\sin\theta - x\cos\theta)} \quad , \qquad \text{Equation 4.6}$$

$$v'(x,y,\theta) = \frac{zD}{R + y\sin\theta - x\cos\theta} \quad , \qquad \text{Equation 4.7}$$

$$U = \frac{R + y\cos\theta - x\sin\theta}{R} \quad . \qquad \text{Equation 4.48}$$

4.4 Algebraic Methods

In general, these methods solve a system of linear equations using iterative methods. Various methods have been investigated and differ from each other by how the algebraic problem is solved.

The reconstruction is accomplished by iteratively updating the unknown linear attenuation coefficients by minimizing the error between the measured and the calculated projection data. In general, all iterative methods have three major steps. The algorithm starts with a forward projection of the volumetric object estimate. It can be initialized with an empty image estimate or with a standard FBP reconstruction to help speed up the reconstruction algorithm's convergence. Then, it compares the forward projection with the real data in order to compute a correction term. Lastly, the correction term is backprojected onto the volumetric object estimate. The process is finished when either the difference between the real data and the estimate is small or when a certain number of iterations is reached. For loss of ambiguity an iteration, without loss of generality, is the processing of all projection data over all projection views exactly once. The number of iterations needed can be calculated with quality measures like the square root of the mean of the squared differences of pixel intensities of two 2D images, or the Pearson correlation coefficient, which measures the linear dependence between two images.
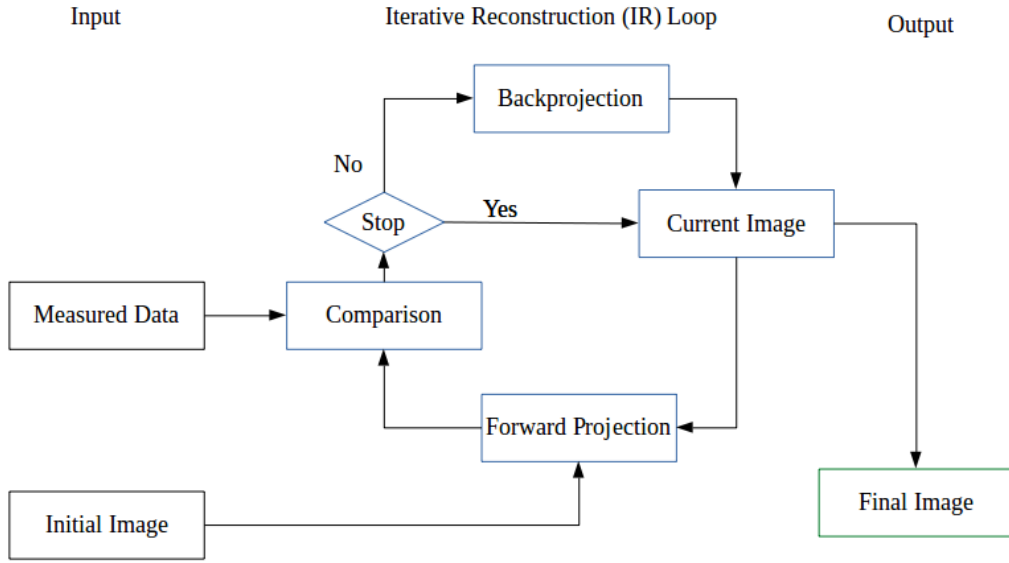
Figure 4.4 Iterative reconstruction process diagram. Adapted from [43].

4.4.1 Simultaneous Algebraic Reconstruction Algorithm

The Simultaneous Algebraic Reconstruction Algorithm (SART) is part of the algebraic reconstruction techniques (ART) family, which uses an iterative method to solve a large system of linear equations. It was proposed by Anderson and Kak in 1984 [44]. A study by Zhang *et al* [45] comparing the SART and BP algorithms, found that BP performed similarly or better than SART for some lesion for the homogeneous phantoms tested, but SART yield better results when using more realistic structured phantoms in terms of in-plane image quality and vertical resolution.

SART updates in one iteration the volumetric object estimates after all rays in one projection view have been processed. The number of updates in one complete iteration of SART is equal to the number of projection views, *N*. Considering the attenuation coefficient of the (k+1)-th iteration is $x_j^{(k+1)}$, that the total of rays in the *n*-th projection view going through the v-th voxel is R_n where the index of all the rays in that projection view is denoted by r $(1 \leq r \leq R_n)$. The update of the linear attenuation coefficient at the *j*-th voxel during processing of the *n*-th projection view is given by

$$x_v^{k+1,n} = x_v^{k+1,n-1} + \lambda \frac{\sum_{r=1}^{R_n} a_{rv,n}\left(\frac{y_{r,n} - \sum_{v=1}^{V} a_{rv,n} x_v^{k+1,n-1}}{\sum_{v=1}^{V} a_{rv,n}}\right)}{\sum_{r=1}^{R_n} a_{rv,n}}$$

Equation 4.9

for $1 \leq v \leq V$, where λ is the relaxation parameter. The relaxation parameter is usually chosen to be between 0 and 1. Therefore, after all N projections have been proceed $x_v^{k+1,n} = x_v^{k+1,N}$.

4.4.2 Maximum-Likelihood Expectation-Minimization

The Maximum Likelihood-Expectation Minimization (ML-EM) algorithm, developed by Dempster *et al* [46], takes into consideration that incident and transmitter photons follow a Poisson distribution. This is a commonly studied method in DBT [47-50]. Zhang *et al* compared in two separate studies the BP, SART, and MLEM algorithms. Using breast phantoms with relevant clinical structures, the BP algorithm was found to lack the ability to reduce out-of-plane artifacts, while both SART and MLEM did reduce these artifacts [47]. In the second study, a simulated reconstructed breast was presented to 5 human observers who found that the detectability of a low contrast lesion was superior for MLEM than SART, and for SART than BP reconstructed images [48]. Tao *et al* [49] evaluated the image quality of DBT images in the reconstruction plane and in depth and found that the ML algorithm resulted in the superior quality, with the information of both high-contrast calcifications and low-contrast tissues well restored. The BP algorithm gave the best SDNR, but the strong interplane artifacts blurred the details of the finding.

The ML-EM algorithm can be divided in two steps. In the first, a likelihood function describing the probability of observing a measurement Y if a certain x is true is obtained (ML step). In the second, an estimative of x, that maximizes the likelihood function, is found (EM step). However, this can be resumed into 3 operations: a forward projection, a comparison, and a backprojection. A forward projection method is used $\left(\sum_t a_{ij} x_t^k\right)$, and then the values are compared to the obtained measurements Y_p through division. The results are summed and weighted by the system matrix elements, a_{pv}, and finally backprojected. The algorithm updates the estimation by multiplying the result of the backprojection by the estimation obtained in the previous iteration. That is,

$$x_v^{k+1} = \frac{x_v^k}{\sum_p a_{pv}} \sum_p a_{pv} \frac{Y_p}{\sum_{v\prime} a_{pv\prime} x_{v\prime}^k}$$

Equation 4.10

It can provide reduced noise in the images when compared to non-statistical methods. Two of the major issues of this algorithm is its stability, since noisy data can easily lead to a noisy solution, due to the comparison by division, and the time.

4.5 Image Postprocessing

Digital imaging processing as a vast range of application. In medical imaging, further postprocessing of the individual DBT slices may be needed to help the interpretation of the images by the radiologist.

4.5.1 Total Variation Minimization Filter

In this dissertation, a 3D Total Variation (TV) minimization method to reduce DBT data noise is used. These TV based minimization algorithms have been researched for its promising results in image denoising [51-54], as they have the ability to preserve edges and reduce noise level simultaneously. The TV minimization problem is described by

$$\min_{u}\{TV(u) + \lambda(u - f\ln u)\} \qquad \textbf{Equation 4.11}$$

where f and u are the original and denoised images, respectively, TV(u) is the total variation of the denoised images, and is a Lagrange multiplier called the regularization parameter, which controls image regularization between removing noise and preserving edges. This last parameter determines the algorithm performance.

CHAPTER 5

Materials and Methods

5.1 Materials

5.1.1 HOLOGIC DBT Unit

The HOLOGIC 3Dimensions® Mammography unit, Fig.5.1, installed at the Hospital da Luz in Lisbon, whose Genius™ 3D Mammography exam offers breast tomosynthesis technology, was used to perform measurements with different acquisition settings.

It has a full field-direct conversion (a-Se) detector which rotates parallel to and with the source. Each square pixel has 70 μm and a binning of 2x2 is used. In a single exam it acquires 15 projections over an arc of 15°, from -7.5° to 7.5°, in 3.7 s. It has a source-to-detector distance of 70 cm, with the detector at the centre of rotation. The unit has an air gap of 25 cm between the detector and the object, which allows the rotation of the detector. In tomosynthesis mode, the x-ray tube has a tungsten (W) target and a 0.7 mm aluminium (Al) filter. The tube has a continuous motion during the acquisition. The software includes a filtered backprojection algorithm to reconstruct the breast tomosynthesis exam.
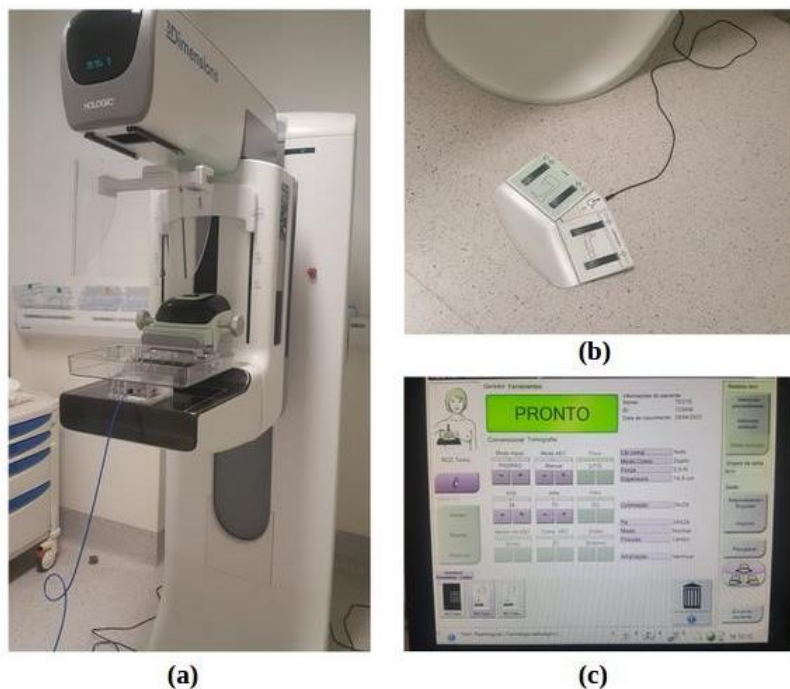
Figure 5.1 HOLOGIC 3Dimension unit installed at Hospital da Luz used. On the left is the whole machine with the phantom and the ionization chamber compressed by the compression paddle. In the right top the pedals that help lowering the paddle were then adjusted manually the kVp and mAs.

5.1.2 Phantom

A PMMA phantom from the Physics department of the Faculty of Sciences of the University of Lisbon was used Fig. 5.2 (a) and (b). It was composed of 4 blocks of width $102,19 \pm 0.01$ mm, hight $108,24 \pm 0.01$ mm and thickness $15,11 \pm 0.01$ mm, of which two were only PMMA, one was made to fit an ionization chamber, and one had aluminium disks to simulate lesions. The disks were numbered from 1 to 12, and their dimensions measured, Tab. 5.1.
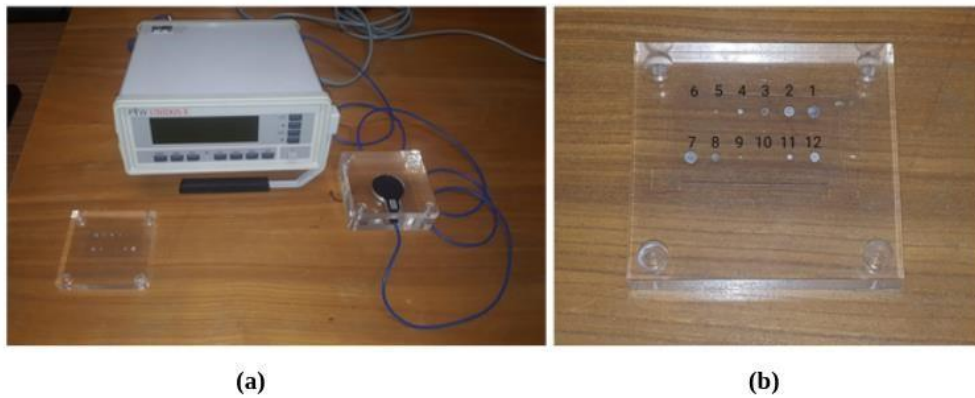
Figure 5.2 Equipment used at the hospital from the Physics department: (a) the electrometer to which the ionizing chamber is connected (blue cable). The ionizing chamber is placed on the corresponding phan-tom block and placed between two PMMA only blocks; (b) block with the aluminium disks and their corresponding numeration.

Table 5.1 Diameter of the aluminium disks of the phantom used in the experimental setup. The block had 12 disks of variable dimensions ranging from 0,68 mm up to 5,16 mm.

	Al disk diameter (mm)	Uncertainty (mm)
1	5,16	
2	4,16	
3	3,24	
4	2,24	
5	1,25	
6	0,68	0,01
7	5,18	
8	3,20	
9	1,04	
10	0,73	
11	2,27	
12	4,14	

5.1.3 Ionizing Chamber

An ionizing chamber was used, Fig. 5.3, to measure air kerma. It was a parallel chamber typically used for diagnostic radiography and mammography. It was a 6 cm^3 Shadow Free Design Mammo Chamber Type 34069 from PTW. It was connected to an electrometer, as can be seen in Fig. 5.2 (a).

Figure 5.3 Parallel chamber ionization chamber from the Physics department used at the Hospital da Luz for the air kerma measurements.

5.2 Methods

5.2.1 Image Acquisition

To evaluate the behaviour of the algorithms for variable doses, several measurements were performed, Tab.5.2. A first measurement was performed using the AEC to choose how to set manually the values during the experiment. The AEC set the tube to 29 kVp and 58 mAs. This acquisition was not used but to evaluate the algorithm parameters that were needed to be defined.

The following acquisitions were done varying first the mAs and then the kVp. The 29 kVp set by the AEC were kept constant while the tube's current was varied in steps of 10 from 70 to 120. Then, the tube's current was kept constant but at the value of 80 mAs, since it was impossible to manually set it back to 58 mAs due to the way it was programmed. The voltage was varied from 21 to 35 kVp in steps of 2. During a first set of measurements, the unit stopped the acquisition due to an error when the tube was set to 33 kVp and 80 mAs. This measurement was ignored, and not repeated.

Table 5.2 Acquisition parameters.

Acquisition	kvp	mAs
AEC	29	58
1	29	70
2	29	80
3	29	90
4	29	100
5	29	120
6	27	80
7	31	80
8	35	80

Two sets of acquisitions varying the voltage and the current separately were performed. The first set of measurements used the two PMMA only blocks with the block of the aluminium disks in between them. The images were saved in a DICOM file and saved in an external disk to later be reconstructed. In the second, the block with the aluminium disks was substituted by the block with the chamber placed in it with the focus upwards, i.e., facing the x-ray tube arm. Care was taken in order to have the cable stably connected to the electrometer across the examination room. Also, knowing the HOLOGIC DBT system takes approximately 3.7 s during one acquisition, a 4 s interval of air kerma acquisition was set on the electrometer. No correction constant was set to take into account the pressure and air temperature in the calculations of the air kerma, as a rough estimate was deemed sufficient.

5.2.2 Image Reconstruction and Postprocessing

5.2.2.1 TIGRE Toolbox

Dr. Ander Biguri developed the open-source Tomographic Iterative GPU-based Reconstruction toolbox (TIGRE) during his PhD at the University of Bath with the support of CERN in 2018 [55].

The toolbox was developed to reduce the gap between end use and algorithm research. It is a 3D tomography reconstruction tool which was optimized to run on GPUs offering tomographic geometry and algorithm development flexibility. It focuses on iterative algorithms and was originally designed for cone beam computed tomography (CBCT) [56].

Current literature and open-source software have significant limitations when reconstructing large images on multiple GPUs. Reconstructing an image with 2000^3 voxels requires 8 of the highest memory GPUs, and 4000^3 voxels requires over 50 GPUs, depending on projection size. Recent GPU based implementation of reconstruction algorithms have tried to overcome this limitation. In the TIGRE toolbox a method for large scale tomography was proposed by Biguri A. [57]. The method makes use of recent advances in memory handling in GPU technology.

The toolbox has a modular architecture, Fig. 5.4, meaning that the two main blocks (in CUDA™ language developed for NVIDIA devices) are independent of the algorithm using it. The algorithms themselves are implemented in a higher-level language (MATLAB® or Python). The communication between the low-level code in CUDA™ and the high-level language code is done using a set of MEX functions.
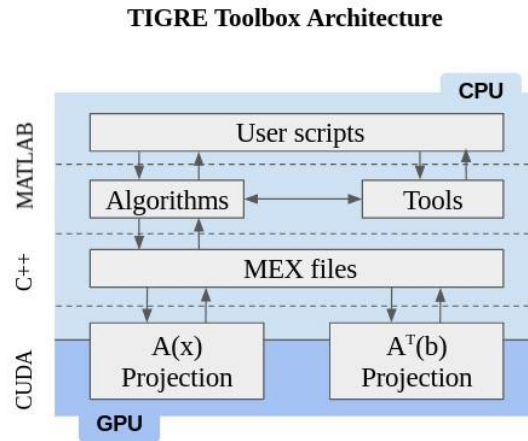

Figure 5.4 Modular architecture of TIGRE toolbox. Adapted from [57].

The Higher-level language used was MATLAB® version 2018. In order to compile the C++ files, the Visual Studio 2017 had to be installed on a computer running on Windows 10. The NVIDIA CUDA version installed was 9.

Several families of algorithms are implemented in the TIGRE toolbox, for example, FDK, MLEM, SART, and SIRT algorithms. As said before, these algorithms are in the high-level language. They were designed to have different parameters (data, geometry, angles, and number of iterations…), and full customization. For each algorithm, a set of parameters which affect its outcome can be set up, allowing the study of its behaviour for different scenarios. However, default values for an easy-to-use application are implemented. Beyond the parameters already mentioned each algorithm has multiple initialization modes, angle ordering schemes, and so on.

All simulations were performed in a system with an Intel® Core™ i7-7700 @ 3.60 GHz CPU, 8 MB Smart Cache; Windows Microsoft Home 10 64-Bit; ASUS GeForce GT1030, 2 GB DDR 5 operating at a speed of 3 GHz, 3 Stream Multiprocessors (SMs), 384 CUDA cores with 1024 parallel threads each.

The geometry in the toolbox is as shown in Fig. 5.5. An x-ray source, S, located at distance DSO from the centre of rotation, O, which coincides with the origin of the cartesian coordinate system, irradiates a cone-shaped region containing the image volume, $\mathbb{I}$. The detector, $\mathbb{D}$, measures the intensity of the detected photons. The image is cantered at O' which is displaced from O by a vector $\overrightarrow{V_{orig}}$ The detector is located at a distance DSD from the source and cantered at D', displaced by a vector $\overrightarrow{V_{det}}$. from D, a point laying in the x-y plane at distance DSD - DSO from the origin. The projection coordinate system uv is defined. The source and the detector rotate around the z-axis during the measurement acquisition. The detector can also rotate about its own centre by 3 axes of rotation. The centre of rotation offset was also implemented, for the case in CT machines where the sample rotates instead of the detector-source system. TIGRE also supports parallel beam geometry, and helical beam geometry.
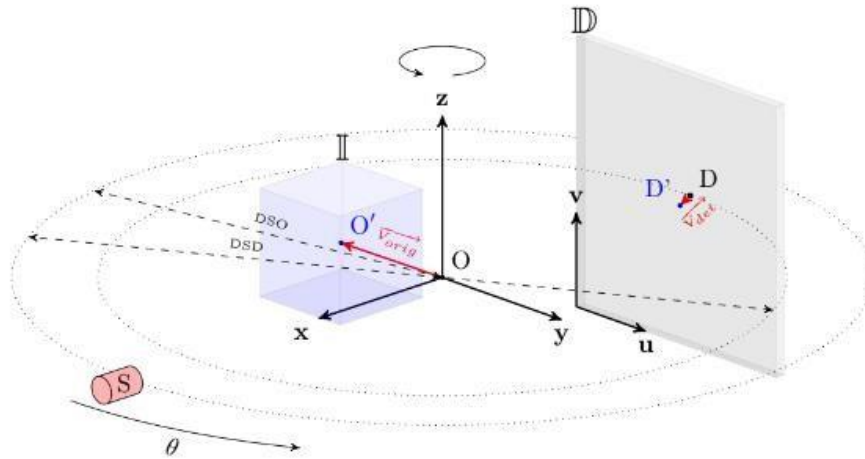

Figure 5.5 Diagram of the geometry of a TIGRE reconstruction.

The geometric variables described are used to perform the operations for image reconstruction.

The building blocks of the toolbox are the projection and back projection operators. These two are optimized for GPU computing with CUDA. Projection is the line integral of the image over the x-ray path, and the backprojection is the "smearing" of the detector data over the image back in the direction of the source. Sampling the image domain in parallel brings better speed performance for the projection operation. For more information on how they were coded, refer to [55-57].

The set of images acquired with the aluminium disks was reconstructed using the TIGRE toolbox code developed in MATLAB. To open the DICOM files, a MATLAB code, which also set the geometry input parameters, was developed. The input parameter of the geometry in the TIGRE toolbox are stored in a structure, were the following:

1. *nVoxel:*   3x1 matrix of number of voxels in the image
2. *sVoxel:*   3x1 matrix with the total size in mm of the image
3. *dVoxel*:   3x1 matrix with the size of each of the voxels in mm
4. *nDetector:*   2x1 matrix of number of voxels in the detector plane
5. *sDetector:*   2x1 matrix with the total size in mm of the detector
6. *dDetector:*   2x1 matrix with the size of each of the pixels in the detector in mm
7. *DSD:*   1x1 scalar value. Distance Source Detector, in mm
8. *DSO:*   1x1 scalar value. Distance Source Origin
9. *offOrigin:*   3x1 matrix with the offset in mm of the centre of the image from the origin
10. *offDetector:*   2x1 matrix with the offset in mm of the centre
11. *rotDetector:*   3x1 matrix with the rotation of the detector in rad by X,Y and Z axis, respectively
12. *COR:*   y direction displacement for center of rotation correction in mm. This can also be defined per angle
13. *mode:*   string defining the geometry type - 'parallel' or 'cone'

In the case of static geometry, that is, when the detector remains stationary in relation to the source, the position of the detector needs to be corrected for each projection. A function is implemented *staticDetectorGeo*(geo,angles), which can be used for DBT systems.

The geometrical parameters were set for the HOLOGIC Selenia Dimensions system, described in the Section 5.1.1, and can be seen in Tab. 5.3. Since it has an air gap which allows the detector to tilt with the x-ray source's movement, the x-ray source is perpendicular to the detector plane during image acquisition, similar to what is observed in CBCT geometries. Therefore, the *staticDetectorGeo*() function was not used. The phantom (black box) has been moved towards the detector plane (red rectangle) using *geo.offOrigin*(). A reconstructed volume of resolution 0.140 mm in the x-y plane and a depth resolution of 1 mm were used.

Table 5.3 Geometry parameters used in the TIGRE Toolbox for the reconstruction of the phantom image acquired with the HOLOGIC 3Dimensions.

Parameter	Value
DSD	700
DSO	700 (Center of rotation at the detector)
dDetector	[0.14, 0.14]
nDetector	[2048, 1280]
sDetector	[286.72, 179.2] (= nDetector $\times$ dDetector)
nVoxel	[45, 2048, 1280]
dVoxel	[1, 0.14, 0.14]
sVoxel	[45, 286.72, 179.2] (= nVoxel $\times$ dVoxel)
offOrigin	[sVoxel(1) / 2- (DSD - DSO) + Airgap), 0, sDetector(2)/2]
offDetector	[0, sDetector(2) / 2]
mode	'cone'

Only the FDK, MLEM and SART algorithms were used.

In the case of the FDK algorithm the filter parameter was the only important one to define. The options available were the Ramp filter, the Shepp-Logan filter, the cosine filter, the Hamming filter, and, lastly, the Hanning filter. The one used in this work's reconstructions was the Hanning filter with a cut-off frequency of 0.2 samples/cycles to minimize the level of noise and homogenize the frequency space samples [59 - 60].

In order to choose the best set of parameters for the algebraic algorithms, some tests were done using the acquisition made with the AEC settings. For the SART algorithm, the choice of angular sampling was first assessed for each angle ordering scheme available in the TIGRE toolbox, namely,

1. ***Random***, where it orders the subset randomly.
2. ***Ordered***, where the subset is used in the input order but divided.
3. ***Angular Distance***, where the next subset is chosen to have the biggest angular distance with the ones used.

Research has shown that in ART, the angle ordering can influence the residual [61- 62], which is the squared norm of the difference between the recorded data and the forward projection of reconstructed image. As such, the ordering angles was tested by measuring the residual per iteration for each of the above schemes. The relaxation parameter was kept constant.

After having tested the ordering schemes, the relaxation parameter's choice was evaluated using the ordering scheme that provided the fastest rate of convergence and smallest residual. Unfortunately, at the current state of knowledge, the choice of relaxation parameter is done by experimentation [61,63-64]. It is known that the choice of a proper relaxation parameter significantly changes the speed at which a solution is found and can avoid infinitely iterating through the same solution in case of an under determined or noisy solution. In TIGRE, two relaxation parameter methods are implemented. The first consists in multiplying the relaxation parameter by a reduction factor after each iteration, and the second is the Nesterov update, which does not technically update the relaxation parameter, but the

image at each iteration using an iteration specific combination ratio of the gradients of the current and previous iterations. The use of both was evaluated.

The number of iterations needed had to be also determined. For that reason, the Root Mean Square (RMSE) was calculated as a function of the number of iterations.

For the case of the ML-EM algorithm it was only important to determine the number of iterations. A similar analysis using the root mean square was performed, Fig. 5.10. However, in this case, an initialization image of an FDK with a Hanning filter was used because the data was noisy and thus the ML-EM would not converge otherwise.

5.2.2.2 Total Variation Minimization Filter

Finally, the reconstructed images using the algorithm with the highest SDNR, were filtered with a Total Variation Minimization Filter (TV), which was developed in MATLAB by Dr. Margarida Mota [58] during her master's thesis at the Institute of Biophysics and Biomedical Engineering (IBEB) in Lisbon. The TV minimization filter code developed, included a comprehensive study of the regularization parameter, λ (set to be constant for all slices). The parameter was set to range from 10 to 200, and the λ value that enabled the greater minimization of TV was used by the TV algorithm. The filtered images were then compared with the ones reconstructed by the HOLOGIC unit software.

5.2.3 Algorithm Performance Analysis

After the reconstruction with the TIGRE toolbox, an in-plane analysis was performed using the Signal Different to Noise Ratio (SDNR), and the Contrast.

The SDNR was calculated with Eq. 5.1,

$$\text{SDNR} = \frac{\mu_D - \mu_B}{\sigma_B} \quad , \qquad \textbf{Equation 5.1}$$

where μ_D and μ_B stand for the mean pixel values in the Region of Interest (ROI) over the biggest disk (disk 1) and background, respectively; and B is the noise, or the standard deviation on the background ROI,

$$Noise = \sigma_B = \sqrt{\text{Variance}} . \qquad \textbf{Equation 5.2}$$

Contrast was calculated as given by Eq. 5.3,

$$\text{Contrast} = \frac{\mu_D - \mu_B}{\mu_D + \mu_B} . \qquad \textbf{Equation 5.3}$$

The SNDR and Contrast were calculated by drawing a circular ROI of the same size for the background and the biggest phantom disk always on the same slice, Fig. 5.6.
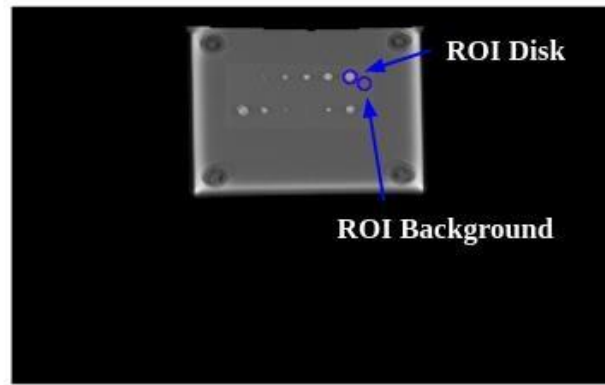
Figure 5.6 ROIs for the in-plane quantitative image analysis.

Moreover, the time each algorithm took on average to perform the reconstruction was measured and compared.

CHAPTER 6

Results and Discussion

6.1 Air Kerma Measurements

The air kerma values measured with the ionizing chamber can be read on Tab. 6.1. As expected, varying the current results in small air kerma changes. On the other hand, small changes in voltage mean that the air kerma increases significantly more rapidly.

Table 6.1 Air kerma (in mGy) measurements for each x-ray tube (current, mAs, and voltage, kVp) parameter used.

kVp	mAs	Air kerma
29	70	2,17
29	80	2,36
29	90	2,59
29	100	2,85
29	120	3,34
27	80	1,96
31	80	2,92
35	80	4,25

6.2 Algorithm Input Selection

As mentioned in the previous Chapter, the parameter for the SART and ML-EM algorithms need to be tested in order to achieve good algorithmically performance (time and reconstruction accuracy).

For SART's algorithm, the order of angular sampling, the relaxation parameter, and the number of iterations were evaluated. As can be seen on Fig. 6.1, using the *Angular Distance* scheme gives the smallest residual after 10 iterations, followed by the *Random* scheme. Such a result was expected since the projections used in the calculations are less correlated when using the *Angular Distance* or *Random* schemes.
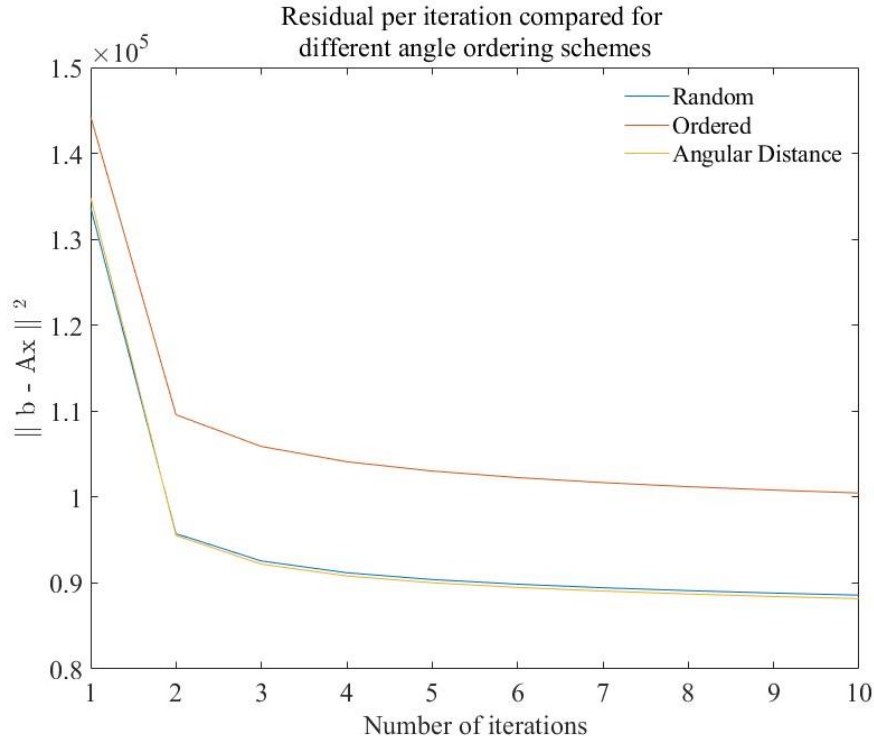
Figure 6.1 Residual per iteration number for SART without relaxation parameter reduction ($\lambda = 1$). Choosing the subset with the biggest angular distance provides the solution with the smallest residual and fastest convergence rate after 10 iterations.

When testing the relaxation parameter options, the results, Fig. 6.2, show that there's little to no difference between the three scenarios evaluated (lambda constant, lambda reduction, and Nesterov update). Lastly, the number of iterations needed had to be determined. For that reason, the RMSE for the lambda reduction and the Nesterov update scenarios was plotted, Fig. 6.3. From this plot, we can see that the use of the Lambda Reduction method is the option to go for. With only 10 iterations the algorithm can converge to a solution. On the other hand, when using the Nesterov update the algorithm does not converge. Hence, when reconstructing the images, the lambda parameter was set to reduce with a constant ratio of r = 0.99 over 10 iterations. In any of these tests the algorithm was initialized with a blank (all zeros) estimation image.
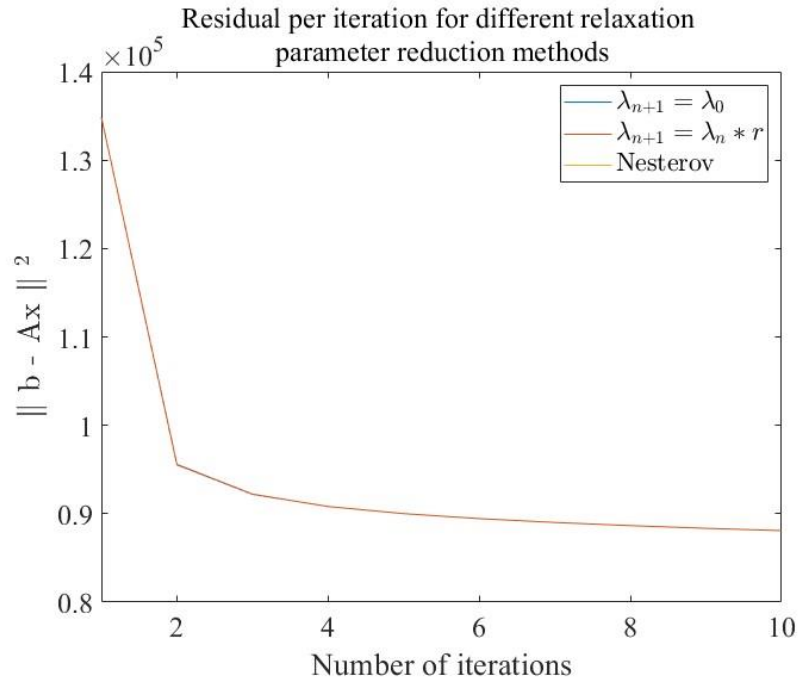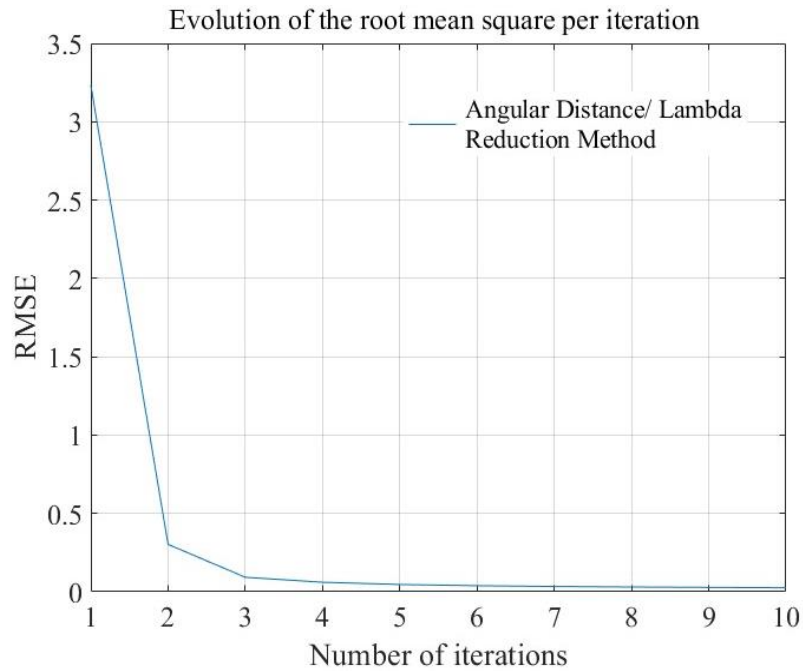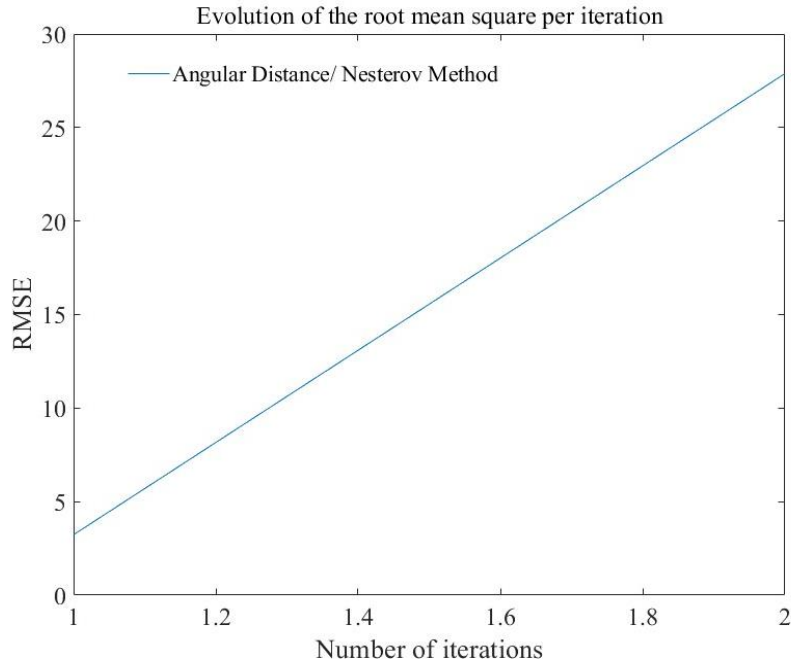
Figure 6.2 Residual per iteration number for SART using two different relaxation parameter methods implemented in the TIGRE Toolbox. The graph shows, for the case of *Angular Distance*, three different scenarios: lambda that is kept constant and equal to unity (b blue), lambda is reduced by a ratio r = 0.99 (red), and lastly the *Nesterov update* (yellow).

(a)

(b)

Figure 6.3 Root mean square error per iteration using the 'Angular distance' angular ordering and (a) the lambda reduction method with a constant ratio r = 0.99, and (b) the Nesterov update. Two quite different behaviours can be observed. Contrary to the lambda reduction method in (a), the RMSE increases linearly when using the Nesterov update (b).

Finally, for the case of the ML-EM algorithm, the number of iterations was determined using the root mean square, Fig. 6.4. However, in this case, an initialization image of an FDK with a Hanning filter was used because the data was noisy and thus the ML-EM would not converge otherwise. It converged quickly, being 2 iterations enough.
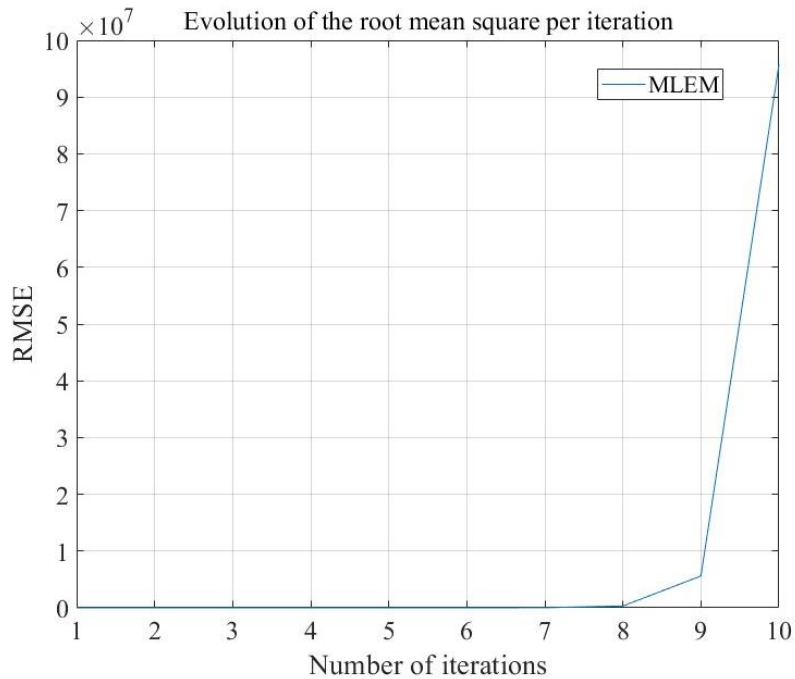
Figure 6.4 Root mean square error per iteration for the MLEM algorithm. With very few iterations the algorithm converges to a solution. If the number of iterations is higher than 8, it diverges rapidly.

6.2 Comparison between algorithms implemented in the TIGRE Toolbox

As was previously mentioned, in this work, the FDK, SART, and MLEM algorithms implemented in the toolbox were first compared. The idea was to test one algorithm of each reconstruction category and evaluate the image quantitatively through an in-plane analysis and measure the time each algorithm takes to reconstruct the data.

A total of 45 slices were generated, from an already pre-processed DICOM file produced by the HOLOGIC system, which simply means that the projection data was already logarithmically transformed. One slice generated by each algorithm used can be seen in Fig. 6.5, for the same tube and current combination (27 kVp/ 80 mAs).
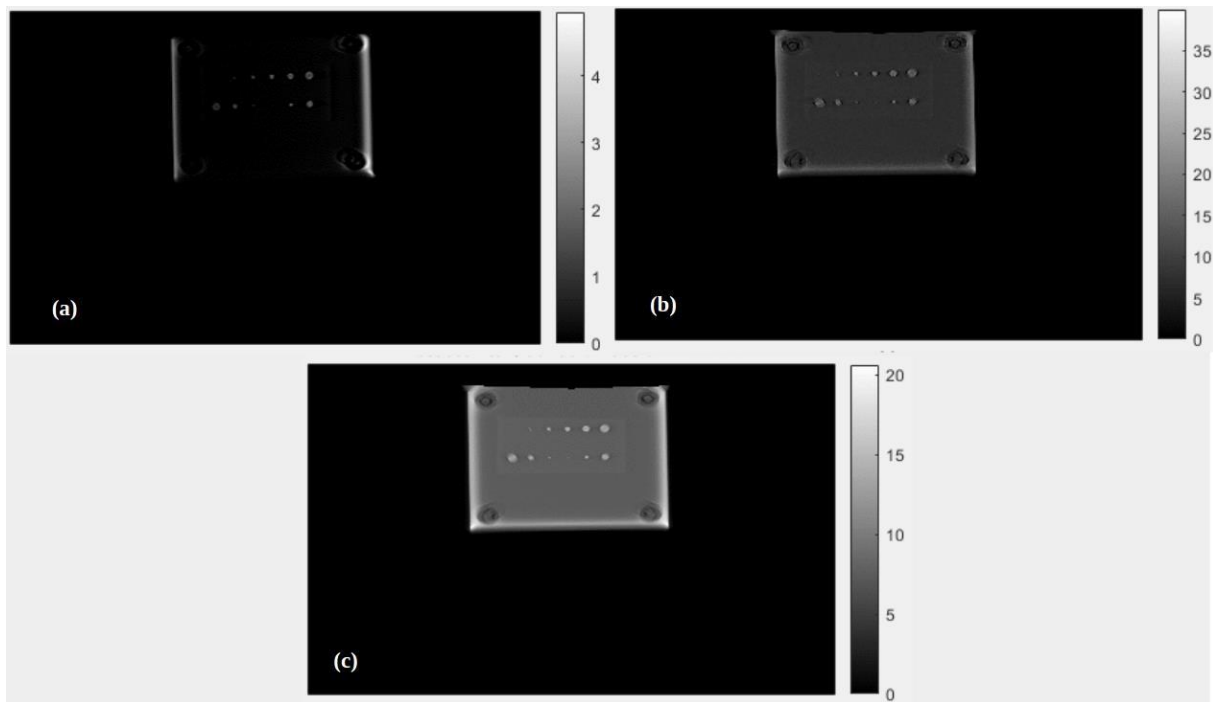

Figure 6.5 Comparison between the same slice (27/45) of the images obtained by each algorithm for a tube voltage of 27 kVp and current 80 mAs; (a) FDK, (b) SART, and (c) MLEM.

Noise and contrast come hand-in-hand when evaluating an image's quality. Images having more contrast, can also display higher levels of noise which decrease the image quality. The two variables were plotted, Fig. 6.6. The FDK algorithm is the one that reconstructs the images with by far the highest contrast and noise values for all the different tube voltage and current settings, when compared with the MLEM and SART algorithms. In fact, one can see that the image reconstructed using the FDK algorithm, Fig. 6.5 (a), is the one with the highest contrast. The tape used in the phantom block with the aluminium disks is barely visible as opposed to what is seen in SART and MLEM reconstruction images. For all the algorithms, the two smallest disks (6 and 10 of Tab. 5.1) were not visible, although the largest of these two (disk 10) was almost visible in every image but in a different slice (slice 33). The disks on the left of the slice have their limits more blurred out than the ones on the right side of the slice, in every reconstruction for each of the algorithms used. The limits of the right-side disks are more well defined in the disk plane of the SART and MLEM reconstruction. However, the blur increases significantly for slices further away from the object plane, Fig.6.7.
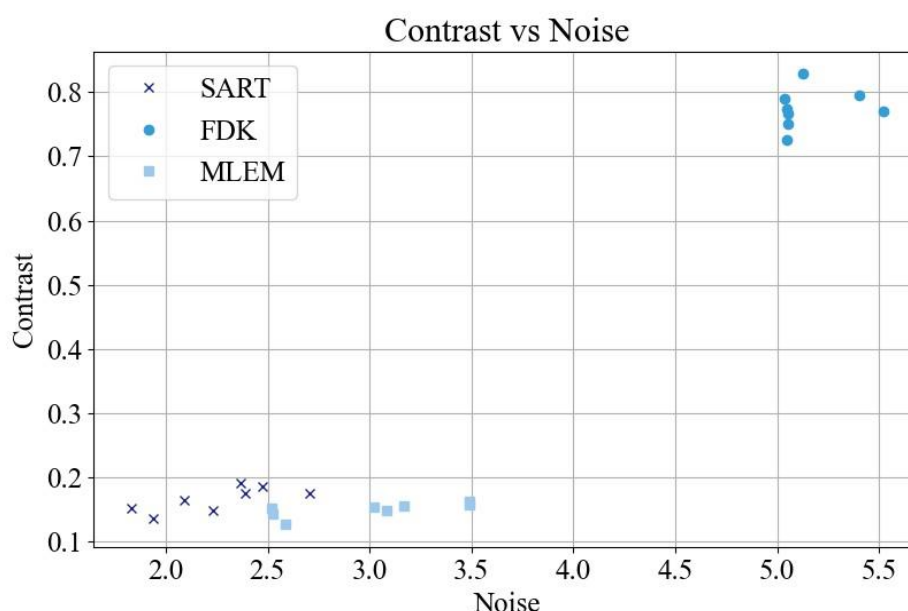

Figure 6.6 Contrast vs Noise graph for the FDK, SART, and MLEM algorithms. Each point, for each algorithm, represents a measurement with different x-ray tube parameters.
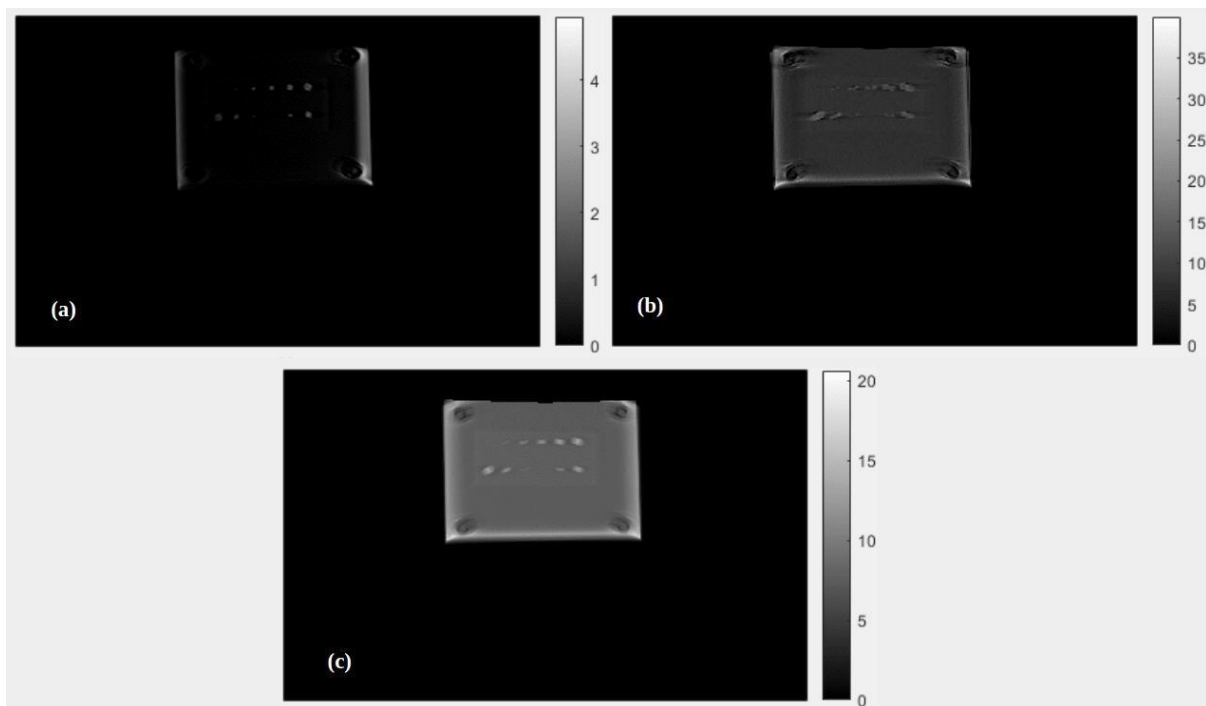
Figure 6.7 Comparison between the same slice (45/45) of the images obtained by each algorithm for a tube voltage of 27 kVp and current 80 mAs; (a) FDK, (b) SART, and (c) MLEM.

   Moreover, the contrast as a function of the tube's current, tube's voltage, and the measured air kerma was plotted, Fig.6.8, 6.9, and 6.10, respectively. In the Fig. 6.8, the voltage is kept constant and equal to 29 kVp, and in the Fig. 6.9 the current is kept constant and equal to 80 mAs. For each algorithm, the contrast is approximately constant as either the current, the voltage, or the air kerma increases. When the tube's current increases, the contrast only decreases slightly for the FDK algorithm, and increases slightly for the SART and MLEM algorithms, Fig. 6.8. When the tube's voltage increases, the contrast diminishes for all the three algorithms, Fig. 6.8.

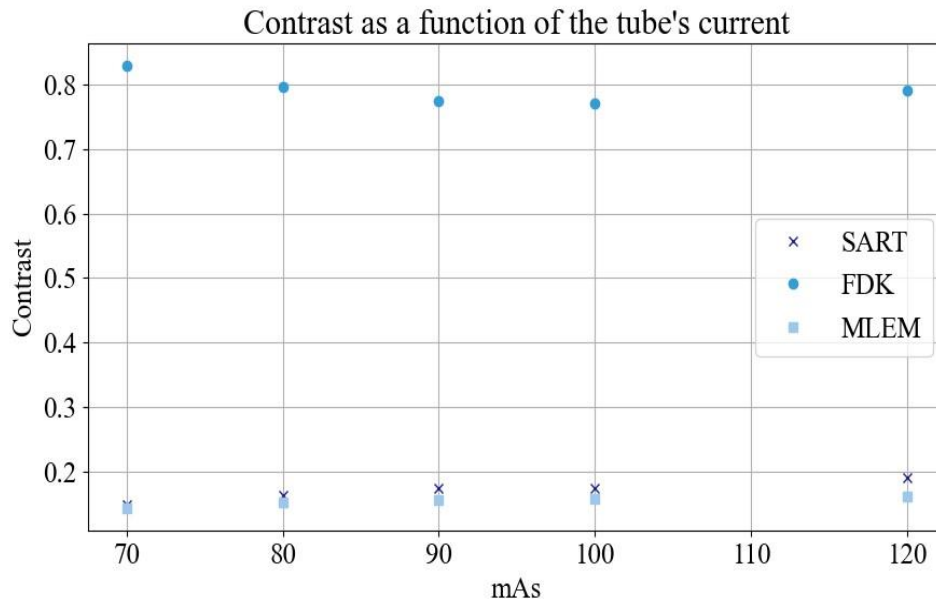**Figure 6.8** Contrast as a function of the tube's current for the FDK, SART, and MLEM algorithms.

Figure 6.9 Contrast as a function of the tube's voltage for the FDK, SART, and MLEM algorithms.

Figure 6.10 Contrast as a function of air kerma measured with the ionization chamber for the FDK, SART, and MLEM algorithms.

As well as the contrast, the SDNR as a function of the tube's current, tube's voltage, and the measured air kerma was plotted in Fig. 6.11, 6.12, and 6.13, respectively. In the Fig. 6.11, the voltage is kept constant and equal to 29 kVp, and in the Fig. 6.12 the current is kept constant and equal to 80 mAs. The lower noise level means that the SDNR was expected to be higher for the algebraic algorithms, as can be seen in the figures. The MLEM and SART algorithms outperformed the FDK algorithm, with the MLEM having the highest SNDR. The MLEM performs best at lower tube voltages, and currents, which in turn translates into a better performance at lower radiation doses.
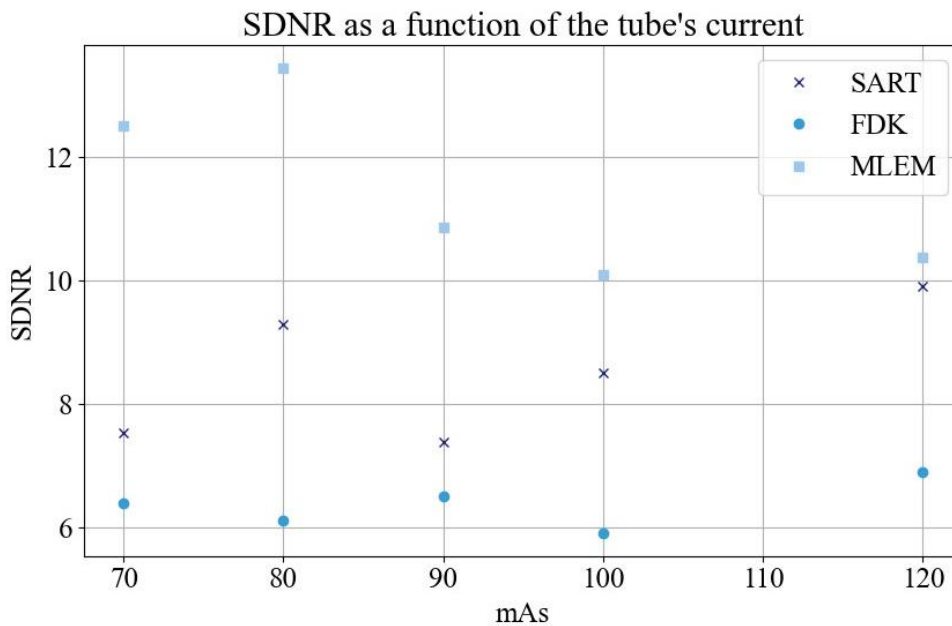
Figure 6.11 SDNR as a function of the tube 's current for the FDK, SART, and MLEM algorithms.
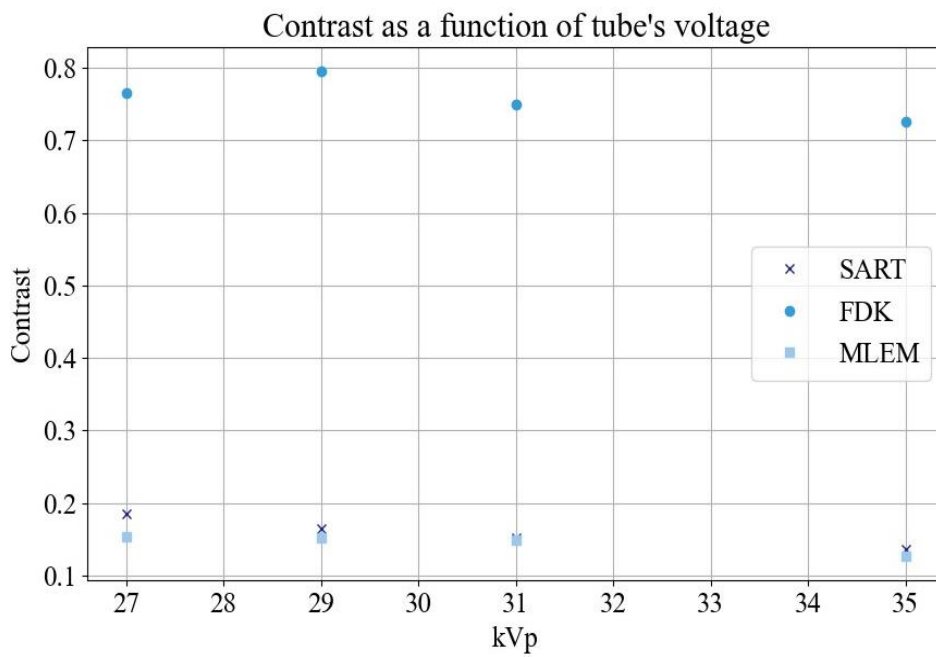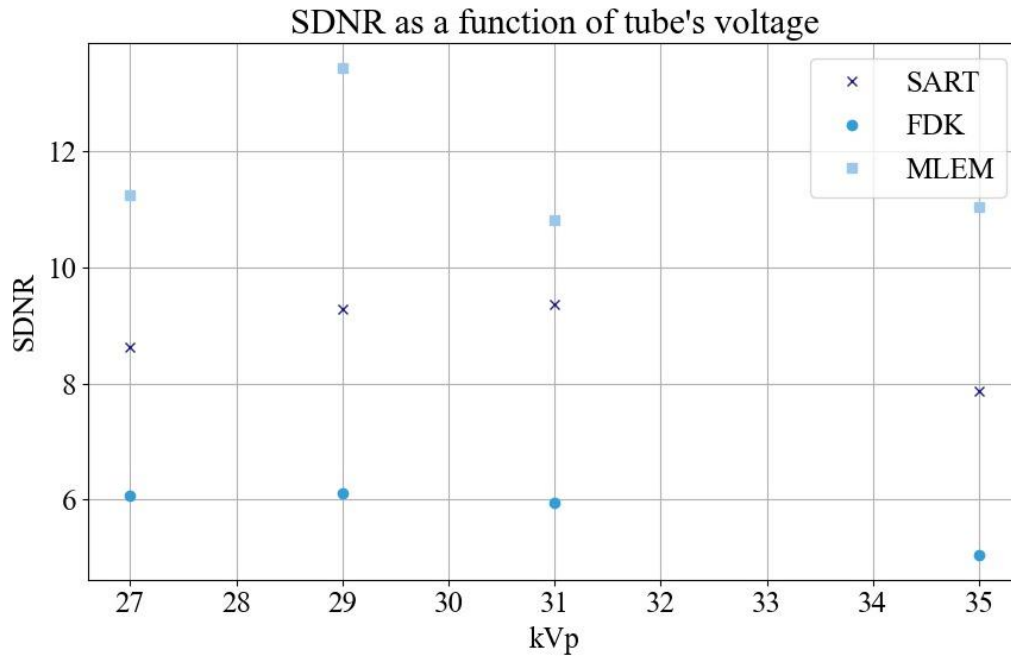
Figure 6.12 SDNR as a function of the tube 's voltage for the FDK, SART, and MLEM algorithms.
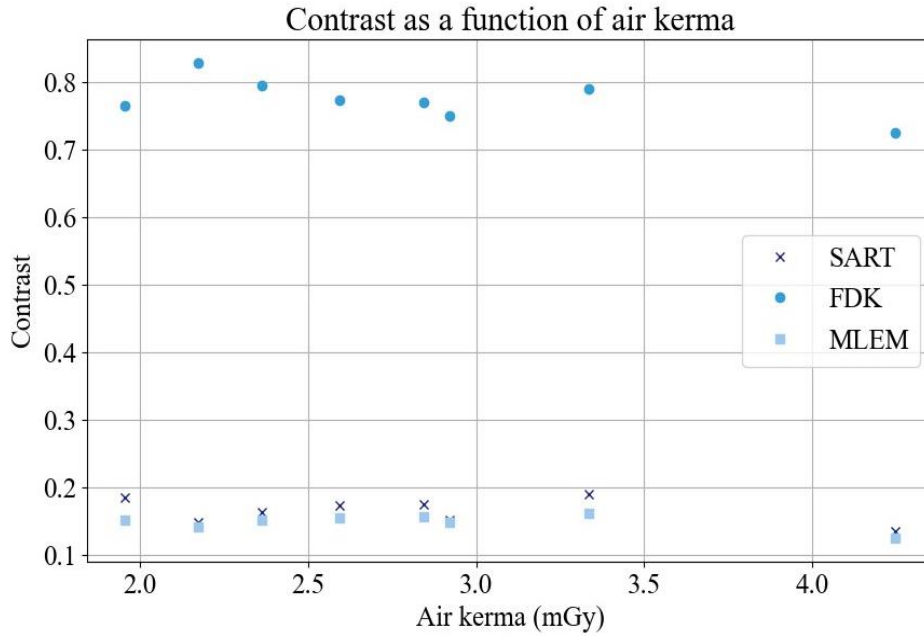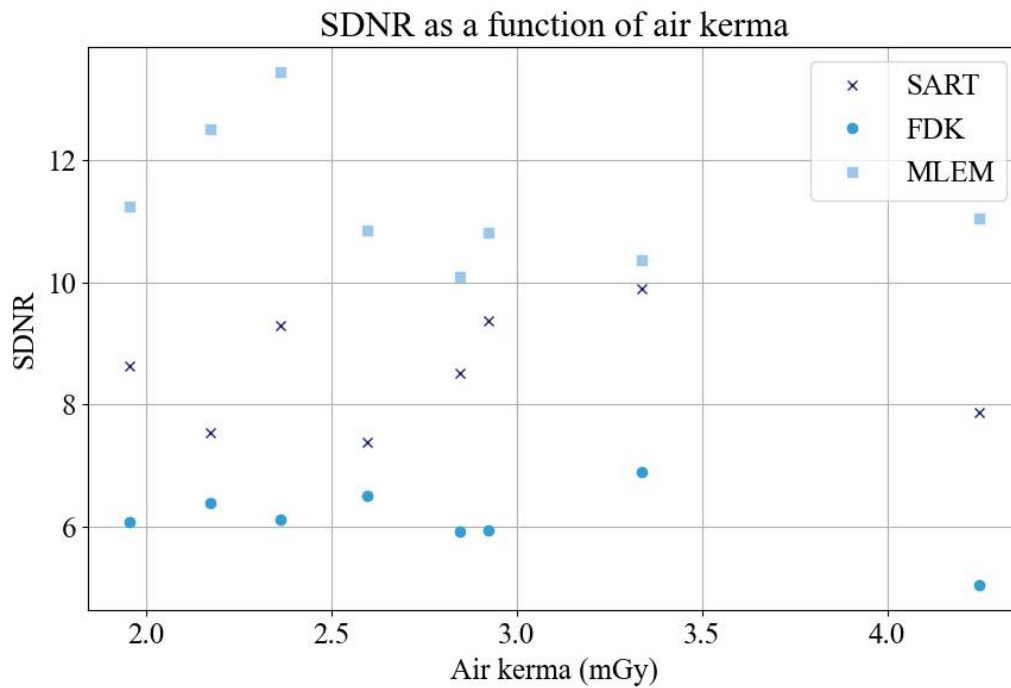

Figure 6.13 SDNR as a function of the air kerma measured with the ionization chamber for the FDK, SART, and MLEM algorithms.

Lastly, the time each algorithm took in total and per iteration, for the case of iterative reconstruction methods, was calculated, Tab. 6.1. For the SART 10 iterations were performed and for the MLEM only 2 iterations were performed, based on Figs. 6.3 (a). and 6.4. The FDK was the fastest, 2.40 s, followed by the MLEM algorithm, 5.78 s. Between the two iterative algorithms, the MLEM took the

41

least amount of time per iteration. It is also worth mentioning that the MLEM converged to a solution faster, requiring fewer iterations than the SART algorithm, contradicting previous studies.

Table 6.2 Time each reconstruction algorithm took for all the different acquisitions and corresponding aver-age. In the case of the iterative reconstruction algorithms, the average time per iteration was also calculated.

kVp	mAs	FDK	MLEM	SART
29	70	2,41	5,80	170,5
29	80	2,43	6,00	168,0
29	90	2,38	5,60	162,3
29	100	2,44	5,70	167,9
29	120	2,40	5,60	164,2
27	80	2,33	5,90	169,8
31	80	2,35	5,80	167,4
35	80	2,43	5,80	167,9
Average time (s)		2,40	5,78	167,25
Number of iterations			2	10
Average time per iteration (s)			2,89	16,73

6.3 Comparison between MLEM and HOLOGIC's software

From the previous results, we can see that the MLEM algorithm outperformed the others in terms of SDNR. The MLEM algorithm reconstructed slices were post-processed with a TV minimization filter, and then compared with the reconstructed and processed images from the HOLOGIC's unit software. This comparison only makes sense after postprocessing the images since the HOLOGIC software most likely has its own post-processing tools.
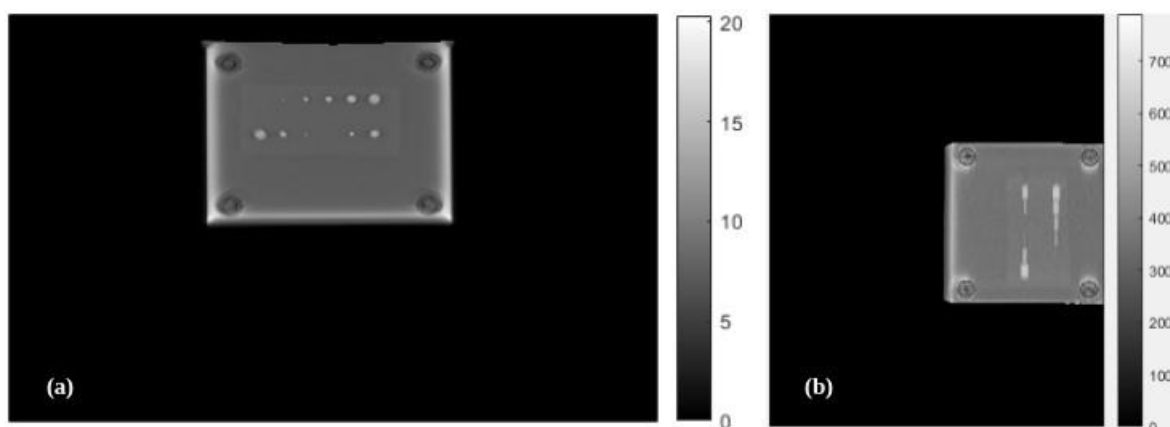

Figure 6.14 Comparison between the images obtained by each algorithm for a tube voltage of 27 kVp and cur-rent 80 mAs; (a) MLEM filtered - slice 27/45 -, (b) HOLOGIC - slice 31/51.

Contrary to the reconstruction done by the HOLOGIC's unit software, a slice of a 1 mm thickness was used. Therefore, in order to compare the two reconstructions, one with 45 slices/ 1 mm thickness another with 51 slices/ 0.8 mm thickness, a fraction rule was used to calculate what slice to use in the HOLOGIC case. The HOLOGIC software has more blur and out of plane artifacts than any algorithm implemented in the TIGRE Toolbox, Fig. 6.14 (b). Compared to the unfiltered reconstruction in the Fig. 6.5 (c), the filtered version has a more homogeneous gray level, Fig. 6.14 (a).

The same quantitative in-plane analysis was done. The contrast and noise were plotted, Fig. 6.15 and this time, only the SDNR was plotted as a function of the tube's current, voltage, and air kerma. In the Fig. 6.16, the voltage is kept constant and equal to 29 kVp, and in the Fig. 6.17 the current is kept constant and equal to 80 mAs.
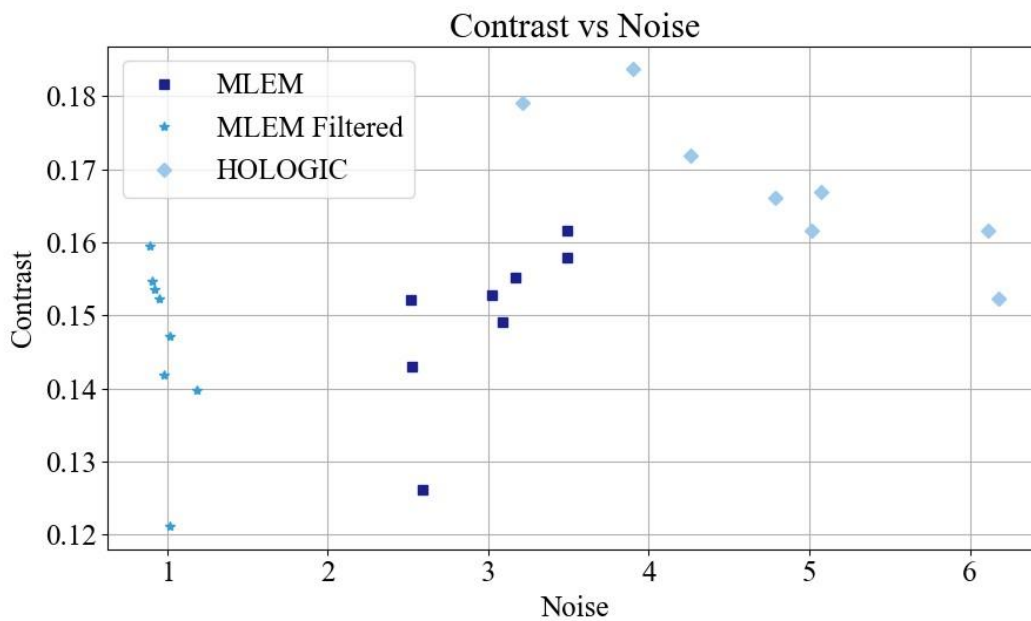

Figure 6.15 Contrast vs Noise plot for the MLEM unfiltered and filtered reconstructions and the HOLOGIC. Each point, for each algorithm, represents a measurement with different x-ray tube parameters.

We can see the effect of the filter in Fig. 6.15. The noise level of the reconstructed image with the filter decreased, more or less, by a factor of 2, while the contrast stayed at the same level with and without filtering. There was approximately ten-fold increase in the SNDR with the filtering. Increasing the tube's current, also increased the SDNR with the TV filtering, opposite to the unfiltered MLEM and the HOLOGIC software reconstruction. On the other hand, with increasing tube voltage, the SDNR decreases if the filter is used. Contrary to the MLEM algorithm, with increasing tube's voltage, the SDNR increases for the HOLOGIC software case.

Using the filter, means that for the same air kerma, it is possible to obtain up to approximately five times the SDNR of that of the HOLOGIC software, Fig. 6.18. On average, the SNDR increased three-fold, and the increase is more significant for lower air kerma values.

Figure 6.16 SDNR as a function of the tube 's current for the MLEM algorithm (filtered and unfiltered), and HOLOGIC's unit software reconstruction.
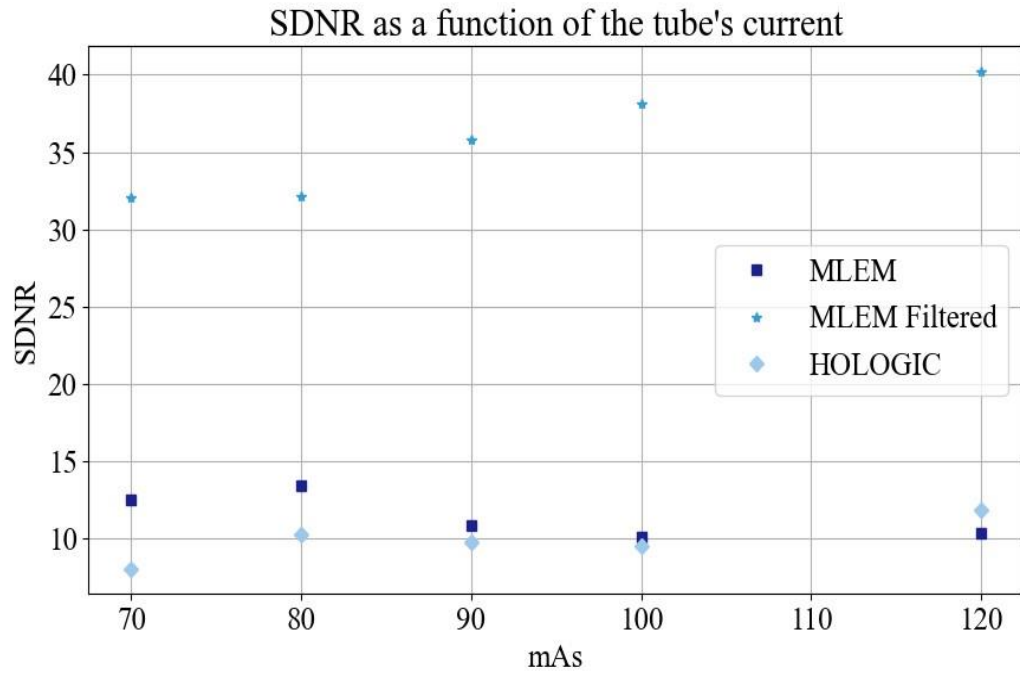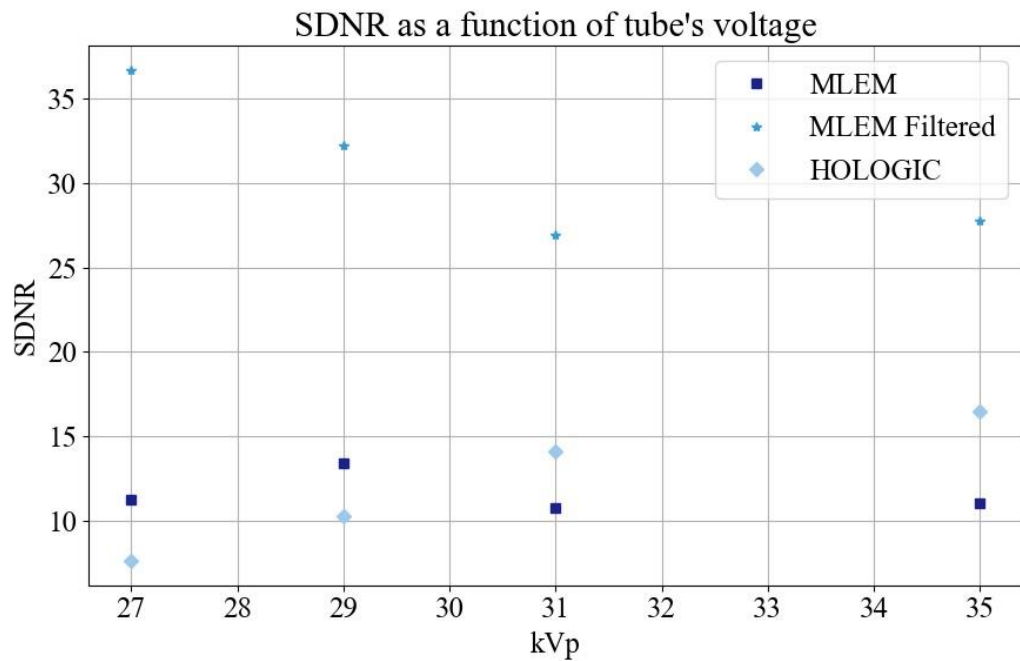

Figure 6.17 SDNR as a function of the tube 's voltage for the MLEM algorithm (filtered and unfiltered), and HOLOGIC's unit software reconstruction.
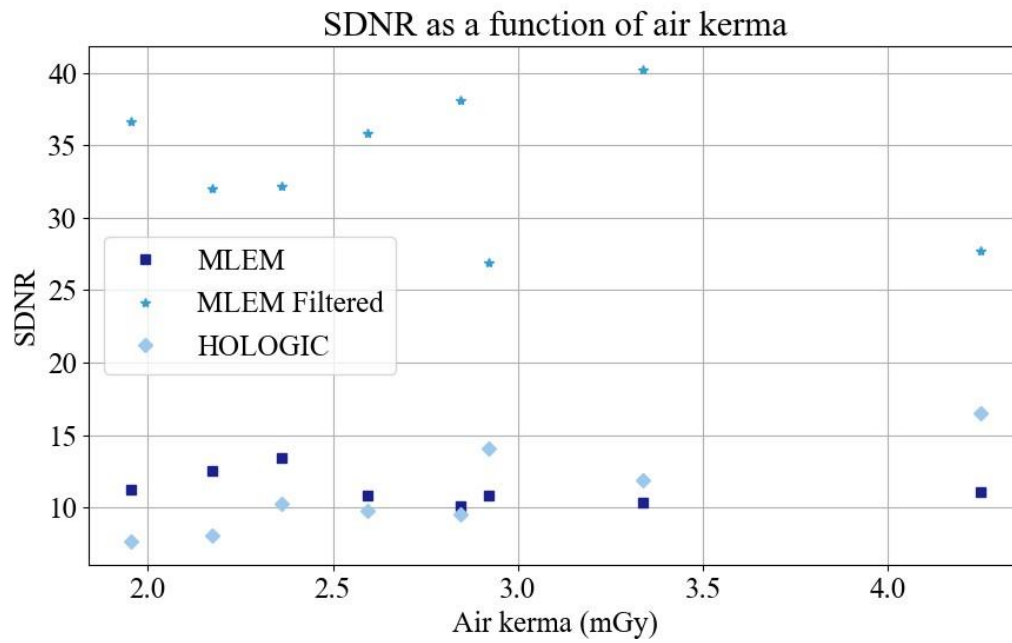
Figure 6.18 SDNR as a function of air kerma measured with the ionization chamber for the MLEM algorithm (filtered and unfiltered), and HOLOGIC's unit software reconstruction.

CHAPTER 7

Conclusion

The goal of this work was to show the potential use of iterative algorithms for dose reduction in breast tomosynthesis applications. To test this, the open-source TIGRE toolbox, which was specially designed to reduce the gap between image reconstruction research and end users of tomography images, was used.

From the in-plane analysis of the FDK, SART and MLEM algorithms used, we can see that the algebraic algorithms showed the highest SDNR in the whole air kerma range of values measured with the ionization chamber. Although these two algebraic algorithms have lower contrast, they benefit from lower image noise. In particular, the statistical algorithm, MLEM, which considers photon statistics, was the one of the two algebraic algorithms that had the best SDNR results. Moreover, contrary to previous studies, the MLEM algorithm was the fastest of the two, taking only 5.78 s and 2 iterations to converge to a solution. Such a result might be due to the fact that the TIGRE toolbox makes use of a multi-GPU approach, a recent improvement. In a previous study, the SART algorithm, in general, had comparable image quality to the ML-convex but required less iterations, contrary to what was found here.

Further studies could explore how the use of other filters, and algorithm settings impact the image quality and running time of these same algorithms implemented in the TIGRE toolbox.

Another goal of this dissertation was to use post-processing tools, in particular, the TV minimization filter, to evaluate the possibility to further reduce the radiation dose to a patient. The MLEM images were then filtered and compared with the ones provided by the HOLOGIC system used at the Hospital da Luz. Both the filtered MLEM images and the unfiltered MLEM images, presented the same contrast level for lower noise levels compared to the ones provided by the HOLOGIC system. In fact, the filter reduced the noise level by a factor of two. Consequently, the filtered MLEM images present for the whole air kerma range a higher SDNR than the HOLOGIC system. Meaning that the combination of the statistical algorithm with the TV minimization filter has an increased advantage over the unfiltered version in potential dose reduction while maintaining or enhancing the in-plane image quality. As for the unfiltered MLEM, it still outperformed the HOLOGIC system at lower air kerma values. From close to 2.9 mGy on, the HOLOGIC system presents a higher SDNR value. However, the image quality in the depth direction, i.e., from x-ray source to detector direction, cannot be quantified with this information. With the SDNR it is only possible to evaluate the algorithm's capability to differentiate details in the image. To study the ability an algorithm has in localizing the structures in the planes along the depth direction, the Artifact Spread Function (ASF), would have had to be measured. The ASF is defined as the ratio between the contrast of the object outside of the plane of its location to that of that in-plane. However, as we could see in Fig. 6.3, blur increased more for the SART and MLEM algorithms than for the FDK algorithm further away from the object plane. However, between the SART and the MLEM, the slices appeared less blurry further from the central

slice in the MLEM reconstruction images, likely due to the use of the FDK initialization with the Hanning filter. The blur is further reduced using the TV minimization filter, however. Furthermore, according to Zhang *et al* [48], the MLEM on phantoms with clinically relevant structures reduced out-of-plane artifacts when compared to the FDK algorithm. This would have been interesting to test by using clinical images in this work.

Breast calcifications in the early stages of breast cancer appear like scattered spots in the mammographic image that range from 0.1 to 1.0 mm in size [65]. With the reconstruction algorithms included in the TIGRE toolbox, it was possible to discern objects bigger than 0.7 mm, which in fact corresponds to the detector's resolution before pixel binning. This is a good result since detecting microcalcifications in such an earlier stage increases the probability of surviving [66]. From the voltage and current graphs, when using the algebraic reconstruction algorithms, it is worth using a higher current around the 70 to 80 mAs, and a lower voltage, below 30 mAs, in the tube in order to obtain higher SDNR and lower radiation doses.

The results have shown that the TIGRE toolbox can be used for DBT image reconstruction. Three of the many reconstruction algorithms available were investigated: FDK, SART, and MLEM. It still has potential for improvements, such as the addition of physical phenomena like scattered radiation and detector noise, as proposed in this review article [67]. Only the non-static DBT geometry was tested, even though it is possible to define a static detection with the TIGRE toolbox. Another unfortunate limitation of this toolbox and of GPU based reconstruction methods in general is the GPU memory. The average computer's GPU has about 2 GB of dedicated memory. In the field of medical imaging, this is by far enough to reconstruct an image with its original resolution. In this work, the MATLAB's function *imresize(A,[numrows numcols])* had to be used to reduce the image to [2048,1280] from [4906,3328]. If a computer with about the same GPU memory as the author of the toolbox (12 GB), had been used, it would not be necessary to reduce the original image size.

Finally, the results obtained in this thesis were positive. However, it would have been ideal to test the algorithms on real DBT images and analyse them. And show the results to a radiologist for evaluation. Moreover, the results show that the use of statistical GPU-based reconstruction algorithms and of a TV minimization filter can potentially be used in DBT in order to reduce the dose to the patient.

References

[1]   Programa de Rastreio de Cancro da Mama - Rastreio e Diagnóstico Precoce. Liga Portuguesa Contra o Cancro. Available at: https://www.ligacontracancro.pt/servicos/detalhe/url/programa-de-rastreio-de-cancro-da-mama/#:~:text=Em%20Portugal%2C%20com%20uma%20p pula%C3%A7%C3%A3o,mulheres%20morreram%20com%20esta%20doen%C3%A7a. [Accessed August 11, 2022].

[2]   Anderson, B., 2021. Breast cancer. World Health Organization. Available at: https://www.who.int/news-room/fact-sheets/detail/breast-cancer [Accessed August 11, 2022].

[3]   Hendrick, R. E. (2010). Radiation Doses and Cancer Risks from Breast Imaging Studies., 257(1), 246–253. doi: 10.1148/radiol.10100570.

[4]   Berger M, Yang Q, Maier A. X-ray Imaging. 2018 Aug 3. In: Maier A, Steidl S, Christlein V, et al., editors. Medical Imaging Systems: An Introductory Guide [Internet]. Cham (CH): Springer; 2018. doi: 10.1007/978-3-319-96520-8_7.

[5]   Jerrold T. Bushberg, J. Anthony Seibert, Edwin M. Leidholdt Jr., John M. Boone; The Essential Physics of Medical Imaging. Lippincott Williams & Wilkins, 2011.

[6]   Duarte, I. C. D (2009). 3D Medical Image Reconstruction. on Digital Breast Tomosynthesis [Master's dissertation, Universidade de Coimbra]. Open access. URI: http://hdl.handle.net/10316/12126.

[7]   Canelo-Aybar C, Ferreira DS, Ballesteros M, et al. Benefits and harms of breast cancer mammography screening for women at average risk of breast cancer: A systematic review for the European Commission Initiative on Breast Cancer. Journal of Medical Screening. 2021;28(4):389-404. doi :10.1177/0969141321993866.

[8]   Holland, R., Mravunac, M., Hendriks, J. H., & Bekker, B. V. (1982). So-called interval cancers of the breast. Pathologic and radiologic analysis of sixty-four cases. Cancer, 49(12), 2527–2533. doi: 10.1002/1097-0142(19820615)49:12<2527::aid-cncr2820491220>3.0.co;2-e..

[9]   Martin, J. E., Moskowitz, M., & Milbrath, J. R. (1979). Breast cancer missed by mammography. *AJR. American journal of roentgenology*, *132*(5), 737–739. doi: 10.2214/ajr.132.5.737.

[10]   B. G. Ziedses des Plantes. "Eine neue methode zur differenzierung in der röntgenographie (planigraphie)," Acta Radiol. **13**, 182–192 (1932). doi: 10.1177/028418513201300211.

[11]   James T. Dobbins III. Tomosynthesis imaging: At a translational crossroads, Medical Physics, Vol. 36, No. 6, June 2009. doi: 10.1118/1.3120285.

[12]   Niklason, L. T., Christian, B. T., Niklason, L. E., Kopans, D. B., Castleberry, D. E., Opsahl-Ong, B. H., Landberg, C. E., Slanetz, P. J., Giardino, A. A., Moore, R., Albagli, D., DeJule,

M. C., Fitzgerald, P. F., Fobare, D. F., Giambattista, B. W., Kwasnick, R. F., Liu, J., Lubowski, S. J., Possin, G. E., Richotte, J. F., … Wirth, R. F. (1997). Digital tomosynthesis in breast imaging. Radiology, 205(2), 399–406. doi: 10.1148/radiology.205.2.9365620.

[13]   Dobbins JT III and Godfrey DJ. "Digital x-ray tomosynthesis: current state of the art and clinical potential," *Phys. Med. Biol.* 2003 Oct 7; 48(19)R65-106. doi: 10.1088/0031-9155/48/19/r01.

[14]   James G. Mainprize, Xinying Wang, and Martin J. Yaffe. "The effect of lag on image quality for a digital breast tomosynthesis system", Proc. SPIE 7258, Medical Imaging 2009: Physics of Medical Imaging, 72580R (13 March 2009); doi: 10.1117/12.811889.

[15]   Poplack, S. P., Tosteson, T. D., Kogel, C. A., & Nagy, H. M. (2007). Digital breast tomosynthesis: initial experience in 98 women with abnormal digital screening mammography. *AJR. American journal of roentgenology*, *189*(3), 616–623. doi: 10.2214/AJR.07.2231.

[16]   Gennaro, G., Toledano, A., di Maggio, C., Baldan, E., Bezzon, E., La Grassa, M., Pescarini, L., Polico, I., Proietti, A., Toffoli, A., & Muzzio, P. C. (2010). Digital breast tomosynthesis versus digital mammography: a clinical performance study. *European radiology*, *20*(7), 1545–1553. doi: 10.1007/s00330-009-1699-5.

[17]   Andersson, I., Ikeda, D. M., Zackrisson, S., Ruschin, M., Svahn, T., Timberg, P., & Tingberg, A. (2008). Breast tomosynthesis and digital mammography: a comparison of breast cancer visibility and BIRADS classification in a population of cancers with subtle mammographic findings. *European radiology*, *18*(12), 2817–2825. doi: 10.1007/s00330-008-1076-9.

[18]   Gur, D., Abrams, G. S., Chough, D. M., Ganott, M. A., Hakim, C. M., Perrin, R. L., Rathfon, G. Y., Sumkin, J. H., Zuley, M. L., & Bandos, A. I. (2009). Digital breast tomosynthesis: observer performance study. *AJR. American journal of roentgenology*, *193*(2), 586–591. doi: 10.2214/AJR.08.2031.

[19]   Rafferty, E. A., Park, J. M., Philpotts, L. E., Poplack, S. P., Sumkin, J. H., Halpern, E. F., & Niklason, L. T. (2013). Assessing radiologist performance using combined digital mammography and breast tomosynthesis compared with digital mammography alone: results of a multicenter, multireader trial. *Radiology*, *266*(1), 104–113. doi: 10.1148/radiol.12120674.

[20]   Smith, A.P., Rafferty, E.A., Niklason, L. (2008). Clinical Performance of Breast Tomosynthesis as a Function of Radiologist Experience Level. In: Krupinski, E.A. (eds) Digital Mammography. IWDM 2008. Lecture Notes in Computer Science, vol 5116. Springer, Berlin, Heidelberg. doi: 10.1007/978-3-540-70538-3_9.

[21]   American College of Radiology (ACR) (2003) Breast Imaging Reporting and Data System Atlas (BI-RADS Atlas). American College of Radiology, Reston

[22]   Saunders, R. S., Jr, Samei, E., Lo, J. Y., & Baker, J. A. (2009). Can compression be reduced for breast tomosynthesis? Monte carlo study on mass and microcalcification conspicuity in tomosynthesis. *Radiology*, *251*(3), 673–682. doi: 10.1148/radiol.2521081278

[23]   Förnvik, D., Andersson, I., Svahn, T., Timberg, P., Zackrisson, S., & Tingberg, A. (2010). The effect of reduced breast compression in breast tomosynthesis: human observer study using clinical cases. *Radiation protection dosimetry*, *139*(1-3), 118–123. doi: 10.1093/rpd/ncq103.

[24]   Zhao, B., & Zhao, W. (2008). Imaging performance of an amorphous selenium digital mammography detector in a breast tomosynthesis system. *Medical physics*, *35*(5), 1978–1987. doi: 10.1118/1.2903425.

[25]   Spangler, M. L., Zuley, M. L., Sumkin, J. H., Abrams, G., Ganott, M. A., Hakim, C., Perrin, R., Chough, D. M., Shah, R., & Gur, D. (2011). Detection and classification of calcifications on digital breast tomosynthesis and 2D digital mammography: a comparison. *AJR. American journal of roentgenology*, *196*(2), 320–324. doi: 10.2214/AJR.10.4656.

[26]   Teertstra, H. J., Loo, C. E., van den Bosch, M. A., van Tinteren, H., Rutgers, E. J., Muller, S. H., & Gilhuijs, K. G. (2010). Breast tomosynthesis in clinical practice: initial results. *European radiology*, *20*(1), 16–24. doi: 10.1007/s00330-009-1523-2.

[27]   Feng, S. S., & Sechopoulos, I. (2012). Clinical digital breast tomosynthesis system: dosimetric characterization. Radiology, 263(1), 35–42. doi> 10.1148/radiol.11111789.

[28]   Eman Shaheen, Nicholas Marshall, Hilde Bosmans, "Investigation of the effect of tube motion in breast tomosynthesis: continuous or step and shoot?," Proc. SPIE 7961, Medical Imaging 2011: Physics of Medical Imaging, 79611E (16 March 2011). doi: 10.1117/12.877348.

[29]   Ingrid S. Reiser, Robert M. Nishikawa, Beverly A. Lau, "Effect of non-isotropic detector blur on microcalcification detectability in tomosynthesis," Proc. SPIE 7258, Medical Imaging 2009: Physics of Medical Imaging, 72585Z (13 March 2009). doi: 10.1117/12.813808.

[30]   Badano, A., Kyprianou, I. S., Jennings, R. J., & Sempau, J. (2007). Anisotropic imaging performance in breast tomosynthesis. *Medical physics*, *34*(11), 4076–4091. doi: 10.1118/1.2779943.

[31]   Chawla, A. S., Lo, J. Y., Baker, J. A., & Samei, E. (2009). Optimized image acquisition for breast tomosynthesis in projection and reconstruction space. *Medical physics*, *36*(11), 4859–4869. doi: 10.1118/1.3231814.

[32]   Sechopoulos, I., & Ghetti, C. (2009). Optimization of the acquisition geometry in digital tomosynthesis of the breast. Medical physics, 36(4), 1199–1207. doi: 10.1118/1.3090889.

[33]   Ren, B. *et al.* (2006). The Dependence of Tomosynthesis Imaging Performance on the Number of Scan Projections. In: Astley, S.M., Brady, M., Rose, C., Zwiggelaar, R. (eds) Digital Mammography. IWDM 2006. Lecture Notes in Computer Science, vol 4046. Springer, Berlin, Heidelberg. doi: 10.1007/11783237_70.

[34]   Van de Sompel, D., Brady, S. M., & Boone, J. (2011). Task-based performance analysis of FBP, SART and ML for digital breast tomosynthesis using signal CNR and Channelised Hotelling Observers. *Medical image analysis*, *15*(1), 53–70. doi: 10.1016/j.media.2010.07.004.

[35]   Robert M. Nishikawa, Ingrid Reiser, Payam Seifi, Carl J. Vyborny, "A new approach to digital breast tomosynthesis for breast cancer screening," Proc. SPIE 6510, Medical Imaging 2007: Physics of Medical Imaging, 65103C (15 March 2007). doi: 10.1117/12.713677.

[36]   Hu, Y. H., & Zhao, W. (2011). The effect of angular dose distribution on the detection of microcalcifications in digital breast tomosynthesis. *Medical physics*, *38*(5), 2455–2466. doi: 10.1118/1.3570580.

[37]   Baorui Ren, Chris Ruth, Tao Wu, Yiheng Zhang, Andrew Smith, Loren Niklason, Cornell Williams, Elena Ingal, Brad Polischuk, Zhenxue Jing, "A new generation FFDM/tomosynthesis fusion system with selenium detector," Proc. SPIE 7622, Medical Imaging 2010: Physics of Medical Imaging, 76220B (18 March 2010);doi: 10.1117/12.844555.

[38]   Sechopoulos I. (2013). A review of breast tomosynthesis. Part I. The image acquisition process. *Medical physics*, *40*(1), 014301. doi: 10.1118/1.4770279.

[39]   Park, J. M., Franken, E. A., Jr, Garg, M., Fajardo, L. L., & Niklason, L. T. (2007). Breast tomosynthesis: present considerations and future applications. *Radiographics : a review publication of the Radiological Society of North America, Inc*, *27 Suppl 1*, S231–S240. doi: 10.1148/rg.27si075511.

[40]   Siddon R. L. (1985). Fast calculation of the exact radiological path for a three-dimensional CT array. *Medical physics*, *12*(2), 252–255. doi: 10.1118/1.595715.

[41]   Suryanarayanan, S., Karellas, A., Vedantham, S., Glick, S. J., D'Orsi, C. J., Baker, S. P., & Webber, R. L. (2000). Comparison of tomosynthesis methods used with digital mammography. *Academic radiology*, *7*(12), 1085–1097. doi: 10.1016/s1076-6332(00)80061-6.

[42]   L. A. Feldkamp, L. C. Davis, and J. W. Kress, "Practical cone-beam algorithm," J. Opt. Soc. Am. A 1, 612-619 (1984). doi: 10.1364/JOSAA.1.000612.

[43]   Soleimani, M.; Pengpen, T. (2015). Introduction: a brief overview of iterative algorithms in X-ray computed tomography. Philosophical Transactions of the Royal Society A: Mathematical, Physical and Engineering Sciences, 373(2043), 20140399–20140399. doi: 10.1098/rsta.2014.0399 .

[44]   H. Andersen and A. C. Kak, "Simultaneous algebraic reconstruction technique (SART): A superior implementation of the ART algorithm," Ultrason. Imaging 6, 81–94 (1984). doi: 10.1177/016173468400600107.

[45]   Yiheng Zhang, Heang-Ping Chan, Berkman Sahiner, Jun Wei, Mitchell M. Goodsitt, Lubomir M. Hadjiiski, Jun Ge, Chuan Zhou, "Tomosynthesis reconstruction using the simultaneous algebraic reconstruction technique (SART) on breast phantom data," Proc. SPIE 6142, Medical Imaging 2006: Physics of Medical Imaging, 614249 (2 March 2006); doi: 10.1117/12.654891.

[46]   Dempster, A. P., Laird, N. M., & Rubin, D. B. (1977). Maximum Likelihood from Incomplete Data via the EM Algorithm. *Journal of the Royal Statistical Society. Series B (Methodological)*, *39*(1), 1–38. http://www.jstor.org/stable/2984875.

[47]   Zhang, Y., Chan, H. P., Sahiner, B., Wei, J., Goodsitt, M. M., Hadjiiski, L. M., Ge, J., & Zhou, C. (2006). A comparative study of limited-angle cone-beam reconstruction methods for breast tomosynthesis. *Medical physics*, *33*(10), 3781–3795. doi: 10.1118/1.2237543.

[48]   Lili Zhou, Jorge Oldan, Paul Fisher, Gene Gindi, "Low-contrast lesion detection in tomosynthetic breast imaging using a realistic breast phantom," Proc. SPIE 6142, Medical Imaging 2006: Physics of Medical Imaging, 61425A (2 March 2006); doi: 10.1117/12.652343.

[49]   Wu, Tao; Moore, Richard H.; Rafferty, Elizabeth A.; Kopans, Daniel B. (2004). A comparison of reconstruction algorithms for breast tomosynthesis. Medical Physics, 31(9), 2636 –2647.doi: 10.1118/1.1786692

[50]   LaRoque, S. J., Sidky, E. Y., & Pan, X. (2008). Accurate image reconstruction from few-view and limited-angle data in diffraction tomography. *Journal of the Optical Society of America. A, Optics, image science, and vision*, 25(7), 1772–1782. doi: 10.1364/josaa.25.001772.

[51]   Mota, A.M., Oliveira, N., Almeida, P., Matela, N. (2016). 3D Total Variation Minimization Filter for Breast Tomosynthesis Imaging. In: Tingberg, A., Lång, K., Timberg, P. (eds) Breast Imaging. IWDM 2016. Lecture Notes in Computer Science(), vol 9699. Springer, Cham. doi: 10.1007/978-3-31941546-8_63.

[52]   Ertas, M., Yildirim, I., Kamasak, M., & Akan, A. (2014). An iterative tomosynthesis reconstruction using total variation combined with non-local means filtering. Biomedical engineering online, 13, 65. doi: 10.1186/1475-925X-13-65

[53]   Chen, Z., Jin, X., Li, L., & Wang, G. (2013). A limited-angle CT reconstruction method based on anisotropic TV minimization. Physics in medicine and biology, 58(7), 2119–2141. doi:10.1088/0031-9155/58/7/2119.

[54]   Kastanis, I., Arridge, S., Stewart, A., Gunn, S., Ullberg, C., Francke, T. (2008). 3D Digital Breast Tomosynthesis Using Total Variation Regularization. In: Krupinski, E.A. (eds) Digital Mammography. IWDM 2008. Lecture Notes in Computer Science, vol 5116. Springer, Berlin, Heidelberg. doi: 10.1007/978-3-540-70538-3_86.

[55]   Biguri, A. (2008). Iterative Reconstruction and Motion compensation in Computed Tomography on GPUs [Doctoral Thesis, University of Bath]. Open access. URI: https://purehost.bath.ac.uk/ws/portalfiles/portal/187963730/main_2_.pdf

[56]   Biguri, A., Dosanjh, M., Hancock, A., and Soleimani, M., TIGRE: a MATLAB-GPU toolbox for CBCT image reconstruction, Biomedical Physics & Engineering Express 2(5), 055010 (2016). doi: 10.1088/2057-1976/2/5/055010

[57]   Biguri A., Lindroos R., Bryll R., Towsyfyan H., Deyhle H., El khalil Harrane I., Boardman R., Mavrogordato M., Dosanjh M., Hancock S., Blumensath T., Arbitrarily large tomography with iterative algorithms on multiple GPUs using the TIGRE toolbox, Journal of Parallel and Distributed Computing 146, 2020, 52-63, 0743-7315, doi: 10.1016/j.jpdc.2020.07.004.

[58]   Mota, A.M., Matela, N., Oliveira, N. and Almeida, P. (2015), Total variation minimization filter for DBT imaging. Med. Phys., 42: 2827-2836. doi: 10.1118/1.4919680.

[59]   Zhao, B., & Zhao, W. (2008). Three-dimensional linear system analysis for breast tomosynthesis. Medical physics, 35(12), 5219–5232. doi: 10.1118/1.2996014.

[60]   Zhao, B., Zhou, J., Hu, Y. H., Mertelmeier, T., Ludwig, J., & Zhao, W. (2009). Experimental validation of a three-dimensional linear system model for breast tomosynthesis. Medical physics, 36(1), 240–251. doi: 10.1118/1.3040178.

[61]   Herman, G. T., & Meyer, L. B. (1993). Algebraic reconstruction techniques can be made computationally efficient [positron emission tomography application]. IEEE transactions on medical imaging, 12(3), 600–609. doi: 10.1109/42.241889.

[62]   Z. Anastasios, Nikolaos M. Freris. (2013). Randomized Extended Kaczmarz for Solving Least Squares. SIAM J. Matrix Anal. Appl. 34, 2 (2013), 773–793. doi: 10.1137/120889897.

[63]   N. Oliveira, A.M. Mota, N. Matela, L. Janeiro, P. Almeida, Dynamic relaxation in algebraic reconstruction technique (ART) for breast tomosynthesis imaging, Computer Methods and Programs in Biomedicine, Volume 132, 2016, Pages 189-196, ISSN 0169-2607, doi: 10.1016/j.cmpb.2016.05.001.

[64]   J. Mesquita; N. Matela; N. Oliveira; M.V. Martins; P. Almeida (2010). Choosing the ART relaxation parameter for Clear-PEM 2D image reconstruction., 98(2), 183–190. doi: 10.1016/j.cmpb.2009.11.010.

[65]   Y. Ma, P. C. Tay, R. D. Adams and J. Z. Zhang, "A novel shape feature to classify microcalcifications," 2010 IEEE International Conference on Image Processing, 2010, pp. 2265-2268, doi: 10.1109/ICIP.2010.5651810.

[66]   Vyborny, C. J., & Schmidt, R. A. (1994). Technical image quality and the visibility of mammographic detail. Syllabus: A Categorical Course in Physics-Technical Aspects of Breast Imaging, AG Haus and MJ Yaffe, Eds. Oak Book III: Radiological Society of North America, 103-111.

[67]   Albert Malet, Diego García Pinto, Josep Fernandez, Robert Martí, Oliver Díaz, "Breast tomosynthesis reconstruction using TIGRE software tool," Proc. SPIE 10718, 14th International Workshop on Breast Imaging (IWBI 2018), 107181L (6 July 2018); doi: 10.1117/12.2317933.